UNIVERSITY OF TURKU

Engineering carbon electrodes for hole-transport-layer-free perovskite solar cells

Department of Mechanical and Materials Engineering

Materials Engineering

Materials of Energy Technology

Master's thesis

Author:

Anna Knol

28.05.2026

Turku

Master's thesis

Subject: Materials Engineering

Author(s): Anna Knol

Title: Engineering carbon electrodes for hole-transport-layer-free perovskite solar cells

Supervisor(s): Dr. Mahboubeh Hadadian, Prof. Kati Miettunen

Number of pages: 62 pages

Date: 28.05.2026

Perovskite solar cells (PSCs) are an emerging photovoltaic technology, demonstrating high power conversion efficiencies. Hole-transport-layer-free (HTL-free) carbon-based PSCs offer advantages of high stability, low material costs, and scalable fabrication techniques, but often face problems with low efficiencies due to poor interface between the perovskite absorber and the carbon electrode. Another advantage of HTL-free carbon-based PSCs is the possibility of recycling them through a facile "revival" process that allows the reuse of the mesoporous scaffold. However, the efficiency of the revival route depends on the integrity of the top carbon electrode. Thus, carbon electrode engineering is of high importance to manufacture efficient, stable, and robust carbon electrodes for HTL-free PSCs.

In this thesis carbon pastes with different inorganic binders were studied to elucidate their effect on power conversion efficiency (PCE), stability, and revival rates of PSCs. Carbon pastes with combinations of ZrO_2 and CuO, MoO_2, NiO, WO_2, WO_3 were manufactured and used to fabricate carbon electrodes for HTL-free PSCs. Carbon electrodes were then characterised with scanning electron microscopy, energy-dispersive X-ray spectroscopy, and 4-point probe conductivity measurements. The performance characteristics of manufactured devices were obtained *via* current-voltage curves and electrochemical impedance spectroscopy. Stability of fabricated cells was assessed through a high-humidity dark storage test. Lastly, revival treatment using γ-valerolactone was applied to the cells and their performance before and after revival was assessed and compared.

Cells with a combination of ZrO_2 and WO_3 were found to have the highest average PCE of 8.8%, closely followed by devices with ZrO_2 and NiO with PCE of 8.7%. Incorporation of CuO and MoO_2 into the carbon paste had a detrimental effect on photovoltaic performance, resulting in PCE of 4% and 1.9%, respectively. The performance of cells with CuO and MoO_2 decreased rapidly during the high-humidity stability test, while the rest of the studied devices exhibited high stability to environmental moisture. Electrodes with MoO_2 detached from the substrate after the revival treatment, while the rest of fabricated electrodes did not show signs of degradation. Revival rates of devices showed high variance between the samples due to variations in the solvent quality.

The results show that the choice of inorganic binders in the carbon paste has an influence on devices performance and stability. Further studies can build upon the present study and investigate the combined effect of champion inorganic binder mixtures with variations of other carbon paste components. Moreover, the results highlight the need for further optimization of the revival treatment of HTL-free carbon-based PSCs.

Keywords: solar cells, carbon electrode, perovskite photovoltaics, recycling

Acknowledgements

I would like to thank my supervisors, Dr. Mahboubeh Hadadian and Prof. Kati Miettunen, for their support and guidance during the research process. I would like to extend my gratitude to Sirius Yli-Paavola for the help with SEM images and EDS analysis. I would also like to thank Dr. Rustem Nizamov for his Python codes that made my life much easier. I am very grateful to Akseli Nykänen from the support team for always being around to help me with the lab stuff and equipment orders. Lastly, special thanks to Tytti, Sirius, and Julianna for the emotional support during our sacred coffee breaks.

Table of contents

Symbols and Abbreviations

C-PSC	carbon-based perovskite solar cell
c-TiO_2	compact titania
DMF	N,N-dimethylformamide
DMSO	dimethyl sulfoxide
EDS	energy dispersive X-ray spectroscopy
EIS	electrochemical impedance spectroscopy
ETL	electron transport layer
FA	formamidinium ($[HC(NH_2)_2]$)
FF	fill factor
FTO	fluorine-doped tin oxide
GBL	γ-butyrolactone
GVL	γ-Valerolactone
HF	high-frequency
high-T	high-temperature
HTL	hole transport layer
HTL-free	hole-transport-layer-free
ITO	tin-doped indium oxide
J_{sc}	short-circuit current density
J-V	current density-voltage
LF	low-frequency
low-T	low-temperature
MA	methylammonium ($[CH_3NH_3]$)
$MAPbI_3$	Methylammonium lead tri-iodide ($MAPbI_3$)
MF	medium-frequency
mp-PSC	mesoporous perovskite solar cells
mp-TiO_2	mesoporous titania
mp-ZrO_2	mesoporous zirconia

MPP	maximum power point
n-i-p	negative-intrinsic-positive
PEDOT:PSS	poly(3,4-ethylenedioxythiophene):poly(styrenesulfonate)
p-i-n	positive-intrinsic-negative
PSC	perovskite solar cell
PV	photovoltaic
R_s	series resistance
R_{HF}	high-frequency resistance
R_{LF}	low-frequency resistance
R_{MF}	medium-frequency resistance
RH	relative humidity
RT	room temperature
SEM	scanning electron microscopy
Spiro-OMeTAD	2,2',7,7'-Tetrakis[N,N-di(4-methoxyphenyl)amino]-9,9'-spirobifluorene
T	temperature
TCO	transparent conductive oxide
V_{OC}	open-circuit voltage

List of Figures

List of Tables

1 Introduction

Climate change is an urgent issue facing humanity in the 21st century, demanding immediate action to reduce its damaging impacts to humans and ecosystems [1]. The goal set by the Paris Agreement is to keep the rise in global average temperature below 2 °C above pre-industrial levels, with efforts to limit it to 1.5 °C, which requires implementation of sufficient measures to mitigate the global warming [2]. Main action lies in curbing the anthropogenic CO_2 emissions through reduced reliance on fossil fuels along with adoption of carbon capture technologies. Substituting fossil fuels with renewable energy sources is a crucial step to cut back the CO_2 emissions [1]. Solar energy is a widely available clean energy source that is playing a big role in energy transition. In 2024, global installed capacity of solar power reached 1860 GW, becoming the most installed renewable energy source [3]. The adoption of photovoltaic (PV) technologies is expected to further increase due to low costs and broad social acceptance [4]. Currently, the market is dominated by crystalline silicon solar panels, which accounted for 98% of total solar energy production worldwide in 2024 [5]. Despite their maturity, there are still challenges associated with crystalline silicon modules, such as their energy-intensive production process and the question of their end-of-life recycling [6].

In recent years, perovskite solar cells (PSCs) have emerged as a potential alternative PV technology. PSCs offer advantages of long carrier-diffusion lengths, high absorption coefficients, and bandgap tunability, allowing the fabrication of PV devices with a variety of different bandgaps [6]. As of 2025, PSCs have achieved record efficiencies of 27.3% and 30.1% for single- and multi-junction cells, respectively [7]. However, despite rapid efficiency advances, there are still issues preventing wide industrial commercialization of PSCs. Main challenges concern the stability of solar cells, their fabrication processes, as well as the problem of maintaining high efficiencies when scaling of devices from laboratory prototypes to large-area modules [8]. Moreover, due to the use of toxic Pb materials, the end-of-life management of PSCs requires careful consideration [9].

PSCs can be fabricated in a variety of different architectures. Conventional planar PSCs can achieve high efficiencies but suffer from poor long-term stability due to the presence of organic hole transport layers (HTLs) and metal electrodes [8]. Alternatively, PSCs devices can be fabricated in the form of triple mesoporous scaffolds consisting of titania, zirconia, and

carbon [10]. These cells do not contain an organic HTL, and the back electrode is made of porous carbon instead of rare metals, such as Au and Ag, which leads to improved stability for this type of architectures [11,12]. Moreover, mesoscopic devices can be manufactured with simple and scalable techniques, while using inexpensive, widely available materials, which reduces the complexity of their commercialization [11]. However, hole-transport-layer-free (HTL-free) carbon-based PSCs (C-PSCs) have lower efficiency than planar cells due to poor contact between the carbon electrode and the functional layers, carbon – perovskite energy level misalignment, and inability of carbon to reflect light [13]. Thus, carbon electrode engineering is essential for improving the performance of carbon-based devices.

One of the proposed strategies for increasing the efficiency of C-PSCs is modifying the work function of the back electrode through incorporation of semiconducting metal oxides into the carbon paste as inorganic binders. The addition of semiconducting inorganic binders facilitates hole transport from the perovskite absorber to the carbon electrode, thereby increasing short-circuit current density (J_{sc}) and open-circuit voltage (V_{oc}) of the cells [14–19]. Materials such as NiO [14–17,20–23], WO_3 [18,19], Mn_3O_4 [24], and Fe_2O_3 [25] have been employed for fabrication of carbon electrodes. Devices with semiconducting metal oxide additives also exhibit better stability due to the particles decreasing the porosity of the electrode which prevents environmental moisture and oxygen from interacting with perovskite absorber [19,25]. Despite a variety of previous studies, a comprehensive comparison of PSC devices with different inorganic binders is missing. Moreover, other materials such as MoO_2 and WO_2 that have not previously been used as carbon electrode additives, could also be employed in carbon pastes with potential to improve the performance of solar cells.

Another concern that has to be addressed before commercialization of PSCs is the recycling of degraded end-of-life devices. Due to the variety and complexity of PSC architectures, developing a single procedure to recycle and recover valuable materials is quite challenging [26]. Common strategies include reviving the entire device, reusing components, recycling constituent materials, and recovering raw materials [9]. Revival is the most energy-efficient strategy from a circular economy perspective due to the entire device architecture remaining intact after the process [9]. The procedure involves washing out the degraded perovskite absorber layer and re-loading it anew, which makes its implementation possible

for HTL-free mesoporous PSCs only. Previous studies on revival of C-PSCs show that the carbon electrode is quite susceptible to damage during the process, lowering the efficiency of recovered devices [27,28]. This further underlines the need for carbon electrode engineering to manufacture robust electrodes able to withstand the revival process and exhibit good performance and lifetime. One of the potential routes for improving the mechanical properties of the carbon electrodes is through the addition of inorganic binders to the carbon paste. Inorganic binders can enhance the hardness of the carbon electrodes and improve their adhesion to the substrate [24]. However, it is still unclear what part can the inorganic binders play in preserving the integrity of the carbon electrodes after the revival treatment.

With that being said, this thesis aims to answer the research question: how do the inorganic binders in the carbon paste affect the performance, stability, and revival of hole-transport-layer-free carbon-based perovskite solar cells? To address this question and achieve the objective of this thesis, carbon electrodes with different inorganic binders were fabricated. Materials employed for manufacturing electrodes were ZrO_2, NiO, CuO, WO_3, WO_2, and MoO_2. The morphology and elemental composition of fabricated carbon electrodes were analysed using scanning electron microscopy and energy-dispersive X-ray spectroscopy. The manufactured devices were characterized through current-voltage measurements, maximum power point tracking, and electrochemical impedance spectroscopy. Stability of fabricated devices was studied through a test in a high-humidity environment under dark storage conditions. A revival procedure was applied to the manufactured devices, and their performance was compared with the performance of the initial devices.

The rest of the thesis is organized as follows: Chapter 2 focuses on an overview of perovskite solar cell technology, device architectures, and recycling options. Chapter 3 talks about carbon electrodes for perovskite solar cells, including high- and low-temperature electrodes, as well as gives insights into the doping of carbon electrodes. Chapter 4 discusses the experimental procedure including materials and methods used in this work. Chapter 5 presents the results of the conducted research work, including their analysis and implications. Finally, Chapter 6 concludes the obtained results.

2 Perovskite solar cells

Perovskite solar cells are an emerging photovoltaic (PV) technology that utilizes perovskite materials as light absorbers. Perovskites are materials with a ABX_3 crystal structure, where A is a large cation, B is a smaller cation, and X is an anion [29]. First perovskite solar cell was developed by Kojima et al. in 2009 using organo-metal halide perovskite and achieved efficiency of 3.81% [30]. In 2012, Kim et al. developed first solid-state PSCs that employed 2,2',7,7'-Tetrakis[N,N-di(4-methoxyphenyl)amino]-9,9'-spirobifluorene (Spiro-OMeTAD) as hole transport layer (HTL) producing efficiency of 9.7% [31]. Significant improvements were achieved in 2013 when Burschka et al. developed a sequential two-step deposition method for perovskite absorbers, resulting in 15% power conversion efficiency (PCE) [32]. In 2014, Zhou et al. achieved efficiency of 19.3% through modification of interfaces within the PSC layers [33]. A new record of 27.3% was set in 2025 for a single-junction cell by a collaborative effort of research groups from Soochow University, UNSW, and Baima Lake [7].

The efficiency improvements raise the question of real-world applications of PSCs in the form of solar cell modules. One of the advantages of PSCs is the diversity of their fabrication techniques. Manufacturing can be done *via* low-cost scalable techniques such as blade coating, slot-die coating, spray coating, inkjet printing, and screen printing, that have low material demands and can proceed in an ambient environment [34]. However, the fabrication of perovskite solar modules comes with a range of reliability concerns associated with upscaling, arising from the nonuniformity of functional layers, reverse bias, and laser scribing [34,35].

In recent years, commercial PSC modules have appeared on the market along with the first large-scale installations. Chinese company MicroQuanta Semiconductor has launched a mass production of 1245 x 635 x 8 mm PSCs modules delivering 100-115 W per piece [36]. MicroQuanta announced the 8.6 MW grid-connected PV plant in 2024, containing over 95 000 perovskite modules [37]. In 2025, another Chinese manufacturer UtmoLight has started mass production of ultra-large PSC modules at the world's first gigawatt-scale perovskite solar module facility [38]. Earlier, UtmoLight unveiled a 450 W PSC module spanning 2.8 m^2 capable of achieving 16.1% efficiency [39]. In Europe, Germany-based company Oxford PV has been producing tandem solar cell modules – devices that combine

silicon and perovskite wafers to achieve higher efficiencies by utilizing a larger share of the solar spectrum [40]. In 2025, the company manufactured modules with 25% efficiency and was planning to start the mass production of tandem cells in 2027 [41].

Despite this, the widespread commercialization of PSCs is impeded by the stability issues. To enter the PV market, PSCs must demonstrate resistance to environmental conditions and pass several operational tests including light soaking, temperature stability, and humidity stability tests. Most of the concerns lie within the absorber layer which is susceptible to degradation due to its intrinsic structural instability. A variety of strategies has been proposed to modify the perovskite layer such as additive and solvent engineering [34].

2.1 Perovskite solar cell components

Conventional PSC devices have a layered structure consisting of an absorber layer sandwiched between two charge carrier transporting layers with electrodes on each side of the cell. The basic scheme of a PSC is presented in Figure 1. Each layer of the device has a specific purpose within the cell. A wide range of materials has been explored for every layer of PSCs to improve efficiency and stability of cells.

Figure 1. Scheme of a conventional perovskite solar cell, FTO – fluorine-doped tin oxide.

Substrate is a transparent base layer of a perovskite solar cell, capable of transmitting light to the absorber. Commonly the substrate is made of glass coated with a transparent conductive oxide (TCO). TCO is a thin layer responsible for conducting the electric charge from the active layers to the external circuit [42]. Materials often used as TCO include fluorine-doped tin oxide (FTO), tin-doped indium oxide (ITO), and zinc oxides. In recent years, flexible polymer substrates gained attention due to interest in utilizing PSCs for wearable electronics [43].

Electron transport layer (ETL) extracts photogenerated electrons from the perovskite absorber and transports them to the electrode, while simultaneously blocking the movement of hole charge carriers to prevent electron-hole charge recombination. ETLs need to have high electron mobility and wide bandgap for efficient electron injection. Commonly used ETL materials include titania (TiO_2) and tin oxide (SnO_2) as well as organic materials such as fullerene and its derivatives in the inverted PSC structures [44].

Perovskite absorber layer plays the crucial role of converting incident light into electron-hole charge carrier pairs. Perovskite materials used in PV are generally organic-inorganic halide perovskites with methylammonium (MA, $[CH_3NH_3]^+$) or formamidinium (FA, $[HC(NH_2)_2]^+$) as large cation (A), lead (Pb^{2+}) as small cation (B), and a halide (Cl^-, Br^-, I^-) as the anion (X) [45].

PSCs are a very appealing PV technology due to the ability to tune their bandgap through compositional engineering. Bandgap determines the range of wavelengths material can absorb and convert into electricity. By substituting A, B, X atoms in the perovskite crystal, it is possible to adjust the energy levels of the absorber to make the bandgap wider or narrower depending on the desired result [46]. The bandgaps of common perovskite absorber materials are presented in Figure 2.

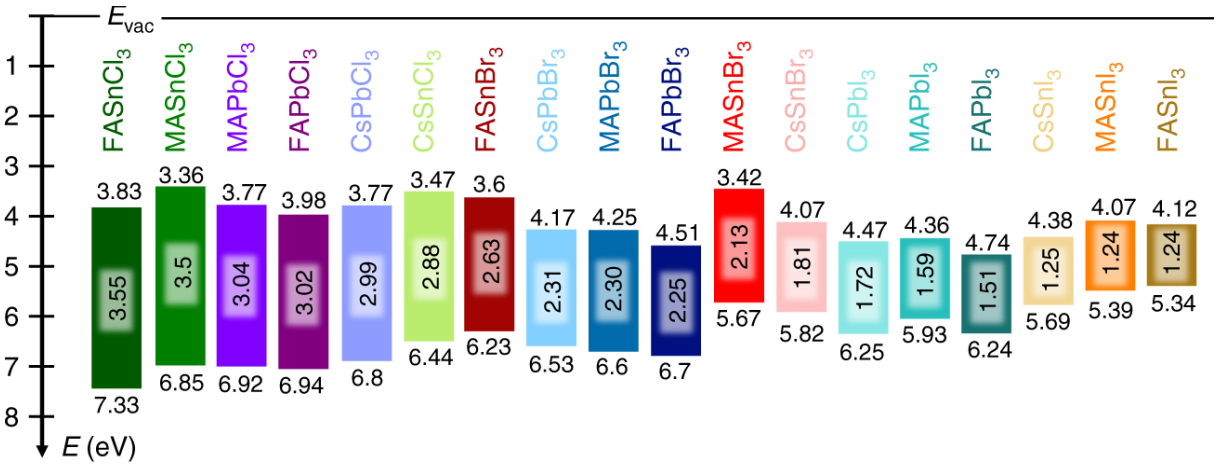

Figure 2. Schematic energy level diagram of perovskite materials. Reproduced from [46] under Creative Commons Attribution 4.0 International License.

A-cation site influences the crystal lattice of the perovskite, which has a direct effect on the stability of the crystal, thereby having an impact on the electronic properties of the material. Meanwhile, exchanging atoms of the B and X sites has a direct influence on the conduction and valence band of the absorber, respectively, as seen in Figure 2 [47].

Methylammonium lead tri-iodide ($MAPbI_3$) is one of the most used perovskite absorber materials. The bandgap of $MAPbI_3$ is shown in Figure 2. However, it is prone to light and oxygen degradation, which significantly affects the stability of PSCs [48]. Replacing MA cations with FA cations has been found to increase the thermal stability of perovskites due to the lower formation of volatile species [35,49]. Another alternative is Cs^+ ions that have been used for synthesizing perovskite absorbers. Cs^+ cations are small, but have low ion diffusion coefficients, which can help increase the stability of devices [50].

High toxicity of lead is another potential challenge preventing the commercialization of PSCs. The EU's Restriction of Hazardous Substances directive sets a limit of 0.1% for the amount lead and its compounds per each homogeneous material in electronic products [51]. Due to this, research has also focused on reducing the amount of lead in PSC devices or replacing Pb-containing perovskites with alternative absorbers. Among the potential candidates are Sn/Ge-based halide perovskites and Sb/Bi-based compounds with perovskite structure [52]. Currently, most promising materials are Sn-based halide perovskites which have similar properties to Pb-based absorbers and show remarkable performance [52]. The bandgaps of common Sn-based perovskites are shown in Figure 2. Despite this, the issue of stability of Sn-based halide perovskite devices in atmospheric conditions persists, preventing their large-scale adaptation [53].

Hole transport layer (HTL) is a counterpart to the ETL, responsible for transport of generated holes to the back electrode along with blocking the passing of electrons. HTLs must have a good charge carrier mobility, thermal stability, and resistance to environmental factors. For normal PSC structures, they must be able to form a film with a strong bond with the perovskite layer underneath without damaging it during the fabrication process [54].

Ever since it was first used in a solid-state PSC in 2012 [31], spiro-OMeTAD has remained the most widely used organic hole transport material for achieving high PCEs in perovskite devices. To increase its hole mobility, spiro-OMeTAD needs to be doped with a combination of lithium bis(trifluoromethylsulfonyl)imide and 4-tert-butylpyridine. However, the addition of dopants accelerates the degradation of PSC devices due to migration of Li^+ ions to the perovskite layer [55,56].

Another organic material commonly employed as a HTL in PSCs is poly(3,4-ethylenedioxythiophene):poly(styrenesulfonate) (PEDOT:PSS). PEDOT:PSS is often used in inverted PSCs due to its high work function and suitable electrical conductivity [57,58]. However, this material is highly corrosive leading to damage to the ITO substrate, which can cause In species to migrate into the perovskite layer, subsequently decreasing the stability of PSCs [59]. Moreover, high level of doping of PEDOT:PSS can lead to recombination of charges at the perovskite/HTL interface, resulting in reduced performance of PSCs [60]. To overcome the stability limitations of organic hole transport materials, several inorganic materials have been explored as HTLs in PSCs, such as NiO, CuI, CuSCN, and WO_x [29,61]. Metal oxides are an appealing option to replace organic materials as they are stable, cheap, and can be fabricated *via* solution-based processes [61,62].

Back electrodes in PSCs have the function of transporting charge carriers to the external circuit. They should have a good electrical conductivity, a suitable work function for efficient charge extraction, and be robust towards environmental factors to protect the perovskite layer from degradation. Noble metals such as Au and Ag have commonly been used as rear electrodes due to their high conductivity. However, these materials have a high cost [63], which is an important factor to consider for commercialisation of PSCs. Thus, some cheaper alternatives have been considered, such as Al, Cu, and Ni. At the same time, metal electrodes can react both with perovskite absorbers and the environment around them, leading to ion migration and unfavourable side products, which in turn result in decreased performance of PSCs [64–66].

Another low-cost material that can be used as a back electrode is carbon. Carbon electrodes are an attractive option due to their price, abundance, tunability, and stability. The hydrophobic properties of carbon can aid in enhancing the moisture resistance of devices, suppressing ion migration in halide perovskites, thereby mitigating their degradation [67]. One drawback of employing carbon rear electrodes is their high sheet resistance, which hinders the charge transport and lowers the efficiency of PSCs [63]. This problem becomes even more prominent in large-area devices [67]. Thus, carbon electrode engineering is required to improve the conductivity of the electrode.

2.2 Perovskite solar cell architectures

The architectures of PSC can be divided into two main groups – normal n-i-p (negative-intrinsic-positive) and inverted p-i-n (positive-intrinsic-negative). These groups can further be divided into subsections of planar and mesoporous solar cells. Schemes of the planar n-i-p, planar p-i-n, and mesoporous architectures are presented in Figure 3. A special type of mesoporous PSCs are hole-transport-layer-free (HTL-free) mesoporous cells. The details of different architectures are discussed in the following subsections.

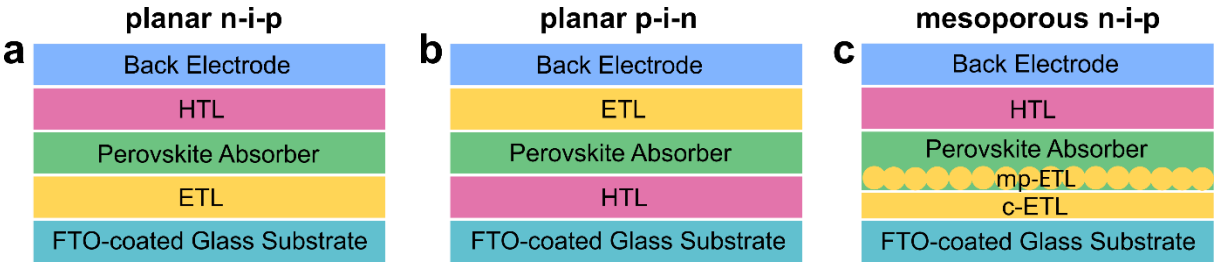

Figure 3. Schemes of most common PSC architectures: a. normal planar n-i-p, b. inverted planar p-i-n, c. mesoporous n-i-p; ETL - electron transport layer, HTL - hole transport layer, c-ETL - compact ETL, mp-ETL - mesoporous ETL, FTO – fluorine-doped tin oxide.

2.2.1 Planar perovskite solar cells

Planar PSCs consist of a flat layered structures with perovskite absorber deposited directly on top of transport layers. Typically, they are made using low-temperature fabrication processes (<150 °C), making them suitable for flexible substrates and scalable roll-to-roll manufacturing [8]. The morphology of the perovskite film must be uniform and homogeneous with minimal defects to reduce recombination and facilitate efficient charge transport [68].

Planar PSCs are divided into two categories based on the arrangement of their layers and electron flow – normal n-i-p and inverted p-i-n devices. In regular n-i-p configuration (Figure 3a), after photogeneration in the intrinsic perovskite absorber layer, electrons are extracted by the n-type ETL and collected by the FTO. On the other side of the cell, holes are transported through the p-type HTL to the back electrode. In inverted p-i-n structures (Figure 3b), the current flow is reversed – holes are transported through the p-type HTL to the FTO, while electrons are collected by the p-type ETL and the back electrode. Traditionally, n-i-p PSCs have been associated with higher efficiencies, while inverted p-i-n

cells have had an advantage of higher stability to environmental factors due to the use of more resilient transport layer materials [8]. In recent years, however the performance gap between n-i-p and p-i-n architectures has decreased [58].

2.2.2 Mesoporous perovskite solar cells

Mesoporous (or mesoscopic) perovskite solar cells (mp-PSCs) build upon dye-sensitized solar cells and utilize mesoporous oxide layers as ETL [29]. In this architecture, the mesoporous scaffold is filled with perovskite (Figure 3c) instead of the absorber layer being formed on top of ETL/HTL layers, as in planar PSCs. As with planar PSCs, mp-PSCs can be fabricated both in a normal n-i-p and in an inverted p-i-n arrangement [8].

One slight drawback of mp-PSCs is the need for high-temperature sintering necessary for the formation of mesoporous layers. Typical fabrication processes are energy-intensive, requiring temperatures of 450-500 °C. This also presents challenges for the fabrication of mp-PSCs on flexible substrates as well as for the roll-to-roll manufacturing [8].

2.2.3 Hole-transport-layer-free carbon-based perovskite solar cells

HTL-free mesoscopic carbon-based perovskite solar cells (C-PSCs) are a special type of mp-PSCs, where HTL removed from the cell stack. The scheme of HTL-free C-PSCs is presented in Figure 4. The bottom electrode is FTO-coated substrate. The substrate is coated with a layer of compact titania (c-TiO_2) that acts as a hole blocking layer. Then, layers of mesoporous titania (mp-TiO_2) and mesoporous zirconia (mp-ZrO_2) are deposited sequentially. mp-ZrO_2 layer acts both as an electrical insulator between ETL and back electrode and as a geometric spacer layer that helps reduce the recombination of charge carriers at back electrode interface [69]. The top electrode is a mesoporous layer made of carbon [70].

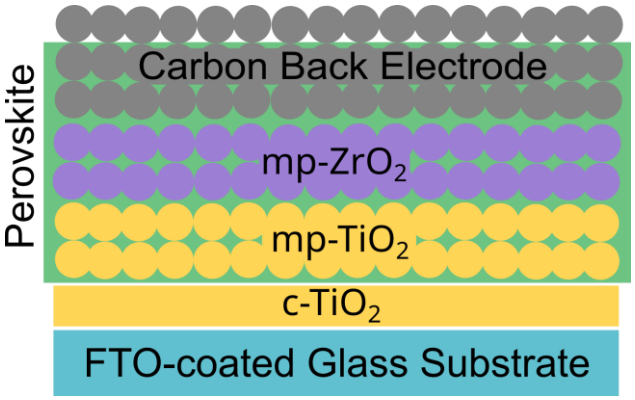

Figure 4. Schematic of HTL-free C-PSC. Perovskite crystals fill the mesoporous scaffold. Back electrode is made of mesoporous carbon. mp-ZrO_2 - mesoporous ZrO_2, mp-TiO_2 - mesoporous TiO_2, c-TiO_2 - compact TiO_2, FTO – fluorine-doped tin oxide.

As illustrated in Figure 4, the mesoporous layers of HTL-free C-PSCs serve as the scaffold to hold the perovskite absorber. The perovskite deposition is the last step of the manufacturing process for mesoscopic HTL-free devices due to the high temperatures required to fabricate the mesoporous layers. The absorber solution can be infiltrated within the scaffold *via* drop-casting, spin-coating, or inkjet printing [15,27,34].

What makes the operation of HTL-free devices possible is the ambipolar nature of halide perovskites as well as the high mobility of charge carriers within carbon – this allows carbon electrode to act as both the HTL and back contact [67]. Elimination of HTL can simplify the manufacturing process of PSCs, reduce fabrication costs, and increase stability of devices. At the same time, due to the absence of HTL the V_{oc} of HTL-free devices is lower, as the energy level mismatch between carbon and perovskite leads to impeded hole extraction and increased recombination losses [70]. One of the strategies for improving the energy level alignment is doping of carbon electrodes, which will be further discussed in Chapter 3.

2.3 Recycling of perovskite solar cells

Recycling of end-of-life devices is crucial for the development and commercialization of PSCs. In 2012, European Union established a directive 2012/19/EU that places the responsibility for collecting and treating PV waste on the panel manufacturers [71]. The directive also highlights the prioritization of product design based on the re-use of PV components and materials.

Due to the diverse variety and complexity of PSCs architectures, developing a single recycling strategy is complicated. Several routes have been proposed, which can be divided into categories based on the recovered economic value of recycled device components and the energy spent during the recycling process [9]. The highest level of PSC recycling is called “revival”, and it involves re-infiltration of the degraded perovskite material, while keeping the rest of the layered structure intact. Since the absorber is the cell layer most susceptible to degradation due to the environmental conditions, it is beneficial to remanufacture it alone. This allows the reuse of the rest of the scaffold, minimizing waste and energy spent on the fabrication of other cell layers that have a longer lifetime. Revival of mp-PSCs was found to be more advantageous than initial manufacturing in terms on energy return on investment and environmental impacts [73]. However, for the process to be profitable revived devices must exhibit good efficiency and stability after the recycling process.

The HTL-free mesoporous scaffold which holds the perovskite – mesopores grant access to the absorber layer, makes it possible to remove it and remanufacture anew. The process can be conducted *via* a liquid treatment where the perovskite layer is dissolved and re-infiltrated anew, using the same solvents commonly utilized for synthesis of perovskite precursor solutions, e.g., N,N-dimethylformamide (DMF), dimethyl sulfoxide (DMSO), or γ-butyrolactone (GBL) [72]. However, some of the common perovskite solvents have issues with toxicity and legality [73]. Alternative solvents have been proposed such as γ-valerolactone (GVL) which is a biomass-derived biodegradable solvent exhibiting low toxicity towards humans, making it an attractive option for future large-scale recycling of PSCs [72]. Previous works have shown that GVL-based revival is a feasible option for remanufacturing of HTL-free mp-PSCs, achieving revival rates of 89% [27]. The importance of a robust back carbon electrode was underlined in the studies as one of the requirements for achieving reproducible results and good efficiencies of revived devices. Defects within the carbon layer can lead to issues with the removal of perovskite during the recycling procedure, while post-treatment damage to the electrode can inhibit uniform re-infiltration of the new perovskite solution. Thus, the optimization of the carbon electrode is required to improve the resilience of HTL mp-PSCs towards the revival process. Carbon electrodes and their composition are further discussed in the following section.

3 Carbon electrodes for perovskite solar cells

As mentioned previously, utilizing carbon as a back electrode presents a better alternative to expensive metals due to its low cost and stability, thus avoiding the stability issues associated with metal migration. The main component of carbon electrodes is flaky graphite and/or carbon black. Carbon materials are usually mixed with an organic and/or inorganic binder and a solvent to form a viscous paste for the deposition of the electrode through techniques such as, for example, doctor-blading or screen-printing. The selection of appropriate paste constituents is important as their characteristics have an influence on the properties of the electrode. For instance, the choice of carbon black influences the porosity, conductivity, and sheet resistance of the paste [74]. The size of graphite flakes affects the porosity and conductivity of the resulting paste [75]. The polymer binders can improve the rheological properties of the mixture to ensure the paste forms a uniform coating during the fabrication process [76,77]. Carbon electrodes in C-PSCs can be divided into two groups based on their preparation routes – low-temperature or high-temperature.

3.1 Low-temperature carbon electrodes

Low-temperature carbon electrodes are typically prepared in the temperature range of 80-110 °C [24,25,78]. Low-temperature manufacturing enables the fabrication of the electrode after the deposition of the perovskite absorber layer. In HTL-free C-PSCs, this type of electrode is deposited directly on top of the perovskite absorber [25]. Since the low-temperature electrode is not mesoporous, liquid-based revival of these devices is not possible. Therefore, other recycling approaches should be used. For example, the electrode can be removed along with the perovskite layer and remanufactured again, while the rest of the mesoporous TiO_2 scaffold is reused [79].

This type of electrodes is advantageous due to faster low-temperature processing without the need for sintering, ability to manufacture planar cells, higher control over perovskite crystallization, and compatibility with flexible substrates [80]. For low-temperature electrodes, the choice of polymer binders has an impact on the performance of devices as well as on the adhesive and mechanical properties of the carbon paste [77].

3.2 High-temperature carbon electrodes

High-temperature carbon electrodes are porous structures that require sintering at high temperatures of 400-550 °C [15,17,81]. High-temperature electrodes are employed in mesoscopic HTL-free C-PSCs. Due to the high-temperature manufacturing process, the perovskite must be deposited after fabrication of the electrode through drop-casting or inkjet printing. Therefore, porosity is one of the key properties of these electrodes, as they should be porous enough for the proper infiltration of the precursor.

The polymer binder materials play a crucial role in formation of a highly porous structure of the high-temperature carbon electrodes. Due to the high-temperature sintering process required for the fabrication of this type of electrodes, most of the organic binder becomes carbonized. This carbonized binder residue assists in the formation of a uniform carbon mesoporous structure with no agglomeration of the solid particles [76].

Inorganic binders are added to the carbon paste to improve the physiochemical properties and to ensure strong adhesion to the layer below [24]. Typically, ZrO_2 nanoparticles are used as the inorganic binder in high-temperature carbon electrodes in HTL-free mp-PSCs to create a good interface with the ZrO_2 spacer layer [76].

3.3 Doping of carbon electrodes

One common strategy for increasing the performance of carbon-based devices in doping the carbon electrodes to modify its work function and increase its hole transport ability [15,18,78]. As mentioned previously, carbon is a low-cost abundant material that could be used as a back contact for PSCs. However, the work function of carbon is too far apart from the valence band of perovskite, resulting in inefficient charge extraction and low V_{oc} [14,24].

A variety of materials have been used as dopants. Heteroatom doping (O, P, B) can induce defects in the carbon matrix resulting in improved interfacial contact and increase the work function of the carbon electrodes [81–84]. Carbon-based single atom materials have been used in C-PSCs to improve V_{oc} of the devices by adjusting the energy level alignment between perovskite absorber and carbon electrode [85].

Another strategy for adjusting the work function of carbon electrodes is through addition of hole transport materials to the carbon paste. The inclusion of inorganic p-type material domains into carbon have been found to aid with hole extraction from the perovskite, subsequently improving the performance of C-PSCs [22,25,86]. Materials such as CuS [86], CuSCN [87], and a variety of oxides – NiO [14–17,20–23], WO_3 [18,19], Mn_3O_4 [24] – have been used as additives to carbon electrodes. Moreover, the addition of other non-HTL oxides such as Fe_2O_3 was also found to improve the photovoltaic performance of C-PSCs due to the improved conductivity of the resulting electrodes [25]. The overview of oxide materials used in C-PSCs is given in Table 1.

Table 1. Overview of oxides used in carbon pastes for C-PSCs.

High-T – high-temperature carbon electrode, low-T – low-temperature carbon electrode, RT – room temperature, *T* – temperature.

Oxide	Electrode type	Oxide content	Top PCE [%]	Stability test conditions	Stability test result	Ref.
NiO	High-T	10, 30, 50%	13.94	-	-	[14]
	High-T	1/10, 1/20, 1/30	8.6	-	-	[15]
	Low-T	-	13.02	dark, *T* = 20 °C, RH = 50-70%, ambient air, unencapsulated, 185 days	94% PCE retained	[20]
	Low-T	-	8.5	-	-	[21]
	High-T	10, 30, 50, 60 wt%	11.82	ambient air, *T* = 20-35 °C, RH = 30-70%, unencapsulated, 1000 hours	85% PCE retained	[16]
	High-T	-	13.2	air, 1000 hours	90% PCE retained	[17]
	Low-T	1:10, 1:20, 1:30	13.26	ambient air, RH = 40%, unencapsulated, 800 hours	85% PCE retained	[22]
	Low-T	2, 5, 8 ‰	12.5	ambient air, RH > 40%, 720 hours	98% PCE retained	[88]
	Low-T	-	14.0	ambient conditions, dark, 600 hours	~90 % PCE retained	[23]

Oxide	Electrode type	Oxide content	Top PCE [%]	Stability test conditions	Stability test result	Ref.
	Low-T	1:30	11.94	-	-	[25]
Fe_2O_3	Low-T	1:30	10.76	-	-	[25]
Fe_2O_3-NiO	Low-T	0.5:0.5:30	13.27	ambient environment, *T* = RT, unencapsulated, 720 hours	82% PCE retained	[25]
CuO	High-T	10%	6.08	-	-	[14]
WO_3	High-T	4 ml of 2.5 wt% ink	10.77	ambient condition, unencapsulated, 150 days	77% PCE retained	[18]
	High-T	5, 7.5, 10 vl% of 2.5 wt% ink	10.3	ambient air, under illumination, 500 h	85% PCE retained	[19]
Mn_3O_4	Low-T	10, 30, 50 wt%	19.03	environmental condition, unencapsulated, 2000 hours	>90% PCE retained	[24]
Co_2O_3	High-T	10%	6.93	-	-	[14]
MoO_3	High-T	10%	0.82	-	-	[14]

As it can be seen in Table 1, a wide range of oxide materials have been used as additives in carbon pastes. However, the presented studies were conducted at different conditions and with a variety of oxide contents. Thus, an overall comparison of carbon pastes with different oxide materials is required to gain insights into the influence of inorganic binders on the performance and lifetime of C-PSCs. Moreover, as previously mentioned, carbon electrodes play an important role in the development of efficient and stable HTL-free mp-PSCs suitable for revival recycling treatment. The utilisation of oxides commonly used as HTLs as binders in carbon pastes presents an opportunity for modifying both the mechanical and electronic properties of carbon electrodes. Oxides can improve the hole transport properties of carbon electrodes, while simultaneously enhancing their hardness and resistance to deformation [24]. Thus, carbon electrode engineering through hole transport oxide materials incorporation is a promising route for developing robust electrodes for stable and efficient HTL-free mp-PSCs.

4 Experimental procedure

4.1 Materials

Carbon monolithic electrodes, mesoporous zirconia electrodes, polyimide impregnation masks, and perovskite precursor solution (includes lead iodide (PbI_2), methylammonium iodide (MAI, CH_3NH_3I), and 5 wt% 5-ammonium valeric acid iodide (5-AVAI) dissolved in γ-butyrolactone (GBL)) were purchased from Solaronix. Zirconium(IV) oxide (ZrO_2, nanopowder, <100 nm particle size), graphite (powder, <20 µm, synthetic), ethyl cellulose (48.0-49.5% (w/w) ethoxyl basis), terpineol (mixture of isomers, for synthesis), γ-valerolactone (GVL, natural, ≥95%, FG), nickel(II) oxide (NiO, 99.99% trace metals basis), molybdenum(IV) oxide (MoO_2, 99%), copper(II) oxide (CuO, 99.999% trace metals basis), tungsten(IV) oxide (WO_2, −100 mesh, 99.99% trace metals basis), tungsten(VI) oxide (WO_3, powder, 99.995% trace metals basis), tungsten(VI) oxide (WO_3, nanopowder, <100 nm particle size (TEM)) were purchased from Merck (Sigma-Aldrich). Carbon black (VXC72) was purchased from Cabot. Ethanol (ETAX Aa, anhydrous, ≥99.5%) was purchased from Anora Industrial.

4.2 Carbon electrode preparation

Graphite, carbon black, zirconia, ethyl cellulose, the selected oxide powder, and 19.5 g of 5 mm stainless steel milling balls were added to a 35 ml jar. Ratios of powders along with their short names are summarized in Table 2.

Table 2. Compositions of fabricated carbon dry paste mixtures.

Name	Graphite	Carbon black	Zirconia	Additional Oxide	Ethyl cellulose
ZrO_2	375 mg	125 mg	50 mg	-	50 mg
ZrO_2 + CuO	375 mg	125 mg	50 mg	50 mg CuO	50 mg
ZrO_2 + MoO_2	375 mg	125 mg	50 mg	50 mg MoO_2	50 mg
NiO	375 mg	125 mg	-	50 mg NiO	50 mg
ZrO_2 + NiO	375 mg	125 mg	50 mg	50 mg NiO	50 mg
ZrO_2 + WO_2	375 mg	125 mg	50 mg	50 mg WO_2	50 mg
nWO_3	375 mg	125 mg	-	50 mg nano WO_3	50 mg
ZrO_2 + nWO_3	375 mg	125 mg	50 mg	50 mg nano WO_3	50 mg
ZrO_2 + WO_3	375 mg	125 mg	50 mg	50 mg WO_3	50 mg

Dry powder mixture was ball milled (MIXER MILL MM 400 from Retsch) for 3 hours at 20 Hz. 1 ml of terpineol was added to the mixture and paste was ball-milled further for 3 hours at 20 Hz. Mesoporous zirconia electrodes were heated to 500 °C for 30 minutes with a 30-minute ramp, then left to cool to 150 °C. Scotch tape (3M, Scotch Magic tape) mask was applied to the electrode to fabricate an electrode area of 12.0 x 15.5 mm^2. Carbon paste was doctor-bladed on top of the electrode using a glass slide, after which the tape mask was removed, and electrode was dried at 100 °C for 10 minutes. Additionally, paste was doctor-bladed onto glass slides for further characterization.

4.3 Carbon electrode characterisation

The sheet resistance of carbon electrode films deposited on the glass slides was recorded with an Ossila Four-Point Probe Test System. Mean sheet resistance values were found by averaging 100 recorded readings from 5 measurement points on the sample film.

The morphology and elemental composition of the samples were analysed by scanning electron microscopy (SEM) (Thermo Scientific Apreo S) and energy dispersive X-ray spectroscopy (EDS) (Oxford Instruments Ultim Max 100 spectrometer). SEM analysis was done at 2kV and 25 pA, using both Everhart-Thornley (ETD) and the lower in-lens (T1) detectors at a 50 mm working distance. EDS analysis was done at 10 kV and 0.4 nA with a 300 mm working distance. EDS spectra were analysed with the AZtec 6.1. software.

4.4 C-PSC fabrication

Carbon electrodes were heated to 450 °C for 30 minutes with a 30-minute ramp. Subsequently, they were cooled to 150 °C, removed from the hot plate, and polyimide masks were applied around the carbon electrode. Next, 5.76 µL of perovskite precursor solution was drop-cast onto the electrodes inside a nitrogen-filled glovebox. Electrodes were then covered with a Petri dish and left for 30 minutes to ensure proper infiltration of the precursor within the mesoporous scaffold. After, Petri dish was removed, electrodes were placed onto a hot plate and annealed at 50 °C for 15 min. Lastly, polyimide masks were removed.

4.5 Device characterisation

Photovoltaic performance of cells was measured using a solar simulator (PEC-L01, PECCELL) under AM 1.5G standard illumination conditions. The cells were illuminated under the solar simulator for 1 minute before the start of measurements. The current density-voltage (J–V) curves were recorded with a Gamry Reference 600+ potentiostat after a 5-second equilibration period in the range from -0.2 V to 1 V in both forward and reverse directions at a scan rate of 100 mV/s with a step size of 20 mV. JV measurements were performed using a custom mask with a rectangular aperture area of 0.64 cm^2.

Maximum power point (MPP) tracking was conducted under illumination using the aforementioned solar simulator and FLUXiM Litos Lite Parallel JV and Stability Measurement Platform with a custom sample holder. Before the measurement, cells were left under illumination for 1 minute, after which a 100 mV/s scan was performed. After a 10 second delay, MPP stressing was conducted for 5 minutes.

Electrochemical Impedance Spectroscopy (EIS) measurements were conducted using the same Gamry potentiostat and the solar simulator used for J–V characterisation. The same sample custom mask with a rectangular aperture area of 0.64 cm^2 was utilized. EIS was carried out in the frequency range from 50 mHz to 5 MHz at open circuit voltage. Before the start of the measurement, initial delay of 60 seconds was applied to stabilize the open-circuit voltage of the samples. Data was analysed using the BioLogic EC-Lab® V11.52 software and fitted to the equivalent circuit diagram shown in Figure 5 to obtain impedance parameters, based on the circuit models employed in [89–92].

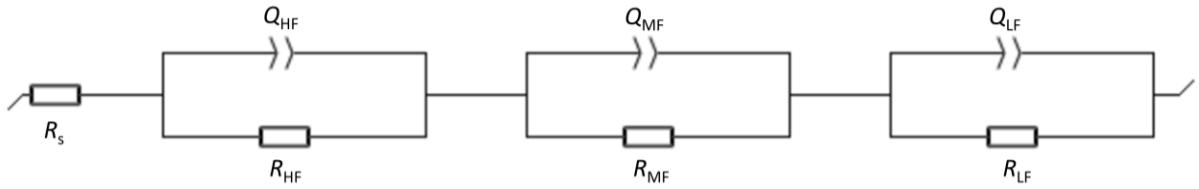

Figure 5. Equivalent circuit diagram for EIS fitting; R_s - series resistance, R_{HF} and Q_{HF} – resistance and capacitance elements associated with high-frequency semicircle, R_{MF} and Q_{MF} – resistance and capacitance elements associated with medium-frequency semicircle, R_{LF} and Q_{LF} – resistance and capacitance elements associated with low-frequency semicircle.

4.6 Stability test

A stability test was conducted in an Aralab TESTA_e CT/TT weather chamber. The test was performed under constant conditions at 25 °C and 85% relative humidity (RH). To monitor the changes in the PCE of devices, they were taken out from the weather chamber for a short period of time to record and an JV scan was recorded under illumination. After, cells were returned into the weather chamber.

4.7 Revival of carbon cells

Revival process was conducted as follows: solar cells were placed into separate petri dishes and 15 ml of GVL was added per each cell until the device structure was fully submerged. Cells were left for 30 minutes until perovskite was dissolved, which was indicated by solvent colour changing from clear to yellow. After, cells were carefully removed and lowered into a beaker with ethanol for 1 minute to wash away the GVL residue. Cells were then dried on a hot plate at 150 °C for 10 minutes. The removal of perovskite was confirmed by an electrical verification using a multimeter. Washed out samples showed voltage of 10-20 mV, which is significantly lower than the voltage of samples with perovskite inside (typically 500-600 mV), confirming the dissolution of the precursor. Then, cells were masked in a fume hood and transferred to a glovebox for infiltration and annealing of the precursor as described in Section 4.4.

5 Results and Discussion

Carbon pastes with different compositions were prepared according to the procedure described in Section 4.2. Perovskite solar cells were then fabricated according to the process described in Section 4.4. Shortly, carbon electrodes were fabricated by doctor-blading the prepared carbon pastes onto commercial zirconia electrodes. Mesoporous zirconia electrodes consisted of a stack of mesoporous layers of FTO/c-TiO_2/mp-TiO_2/ZrO_2. After sintering of the electrodes, perovskite precursor solution was infiltrated into the mesoporous scaffolds and annealed to form $MAPbI_3$ perovskite crystals. Several batches of cells were fabricated to ensure the reproducibility of the obtained results. Commercial carbon electrodes with the same structure were used as a reference.

5.1 Characterisation of carbon electrodes

The sheet resistance of fabricated doped electrode film was measured with a four-point probe. The results are presented in Table 3.

Table 3. Mean sheet resistance values of carbon electrodes.

Thickness of prepared carbon films was ~20 µm. Commercial paste mean sheet resistance is ≤25 Ω/sq for ~15 µm thick layer, value obtained from [93].

Electrode	Mean Sheet Resistance [Ω/sq]
ZrO_2	6.3 ± 0.2
ZrO_2 + CuO	6.7 ± 0.8
ZrO_2 + MoO_2	8.0 ± 0.6
NiO	7.0 ± 0.5
ZrO_2 + NiO	6.5 ± 0.4
ZrO_2 + WO_2	7.4 ± 0.5
nWO_3	6.3 ± 0.3
ZrO_2 + nWO_3	6.7 ± 0.6
ZrO_2 + WO3	7.2 ± 0.5

As it can be observed from the obtained results in Table 3, mean sheet resistance values between fabricated electrodes were quite similar to each other. For all the prepared pastes the mean sheet resistances were smaller than the reported value for the commercial carbon paste. Mean sheet resistances of ZrO_2 and nWO_3 pastes were 6.3 Ω/sq, showing that ZrO_2 nanoparticles can be replaced by WO_3 nanoparticles without changing the resistance of the

electrode. However, when ZrO_2 was replaced by NiO, mean sheet resistance increased to 7.0 ± 0.5 Ω/sq, which may be attributed to the changes in the particle-particle connectivity within the paste. In fact, for all pastes where ZrO_2 and another oxide were mixed, the mean sheet resistance increased compared to the paste with ZrO_2. Moreover, despite the metal-like electrical conductivity of MoO_2, the ZrO_2 + MoO_2 paste had the highest mean sheet resistance of 8.0 ± 0.6 Ω/sq. It is possible that MoO_2 oxidised to MoO_3 during the high-temperature sintering of carbon electrodes [94,95], thus becoming a semiconducting material.

Top-view SEM was performed to study the surface morphology of fabricated carbon electrodes on top of C-PSCs. Images taken with T1 detector highlight the contrast between elements as heavier elements appear brighter than light ones. Bright large circular spots observed in Figure 6 are the perovskite domains formed within the carbon electrode after the precursor infiltration. Darker regions are the carbon black/graphite mixture, and small dots within are the oxide materials.

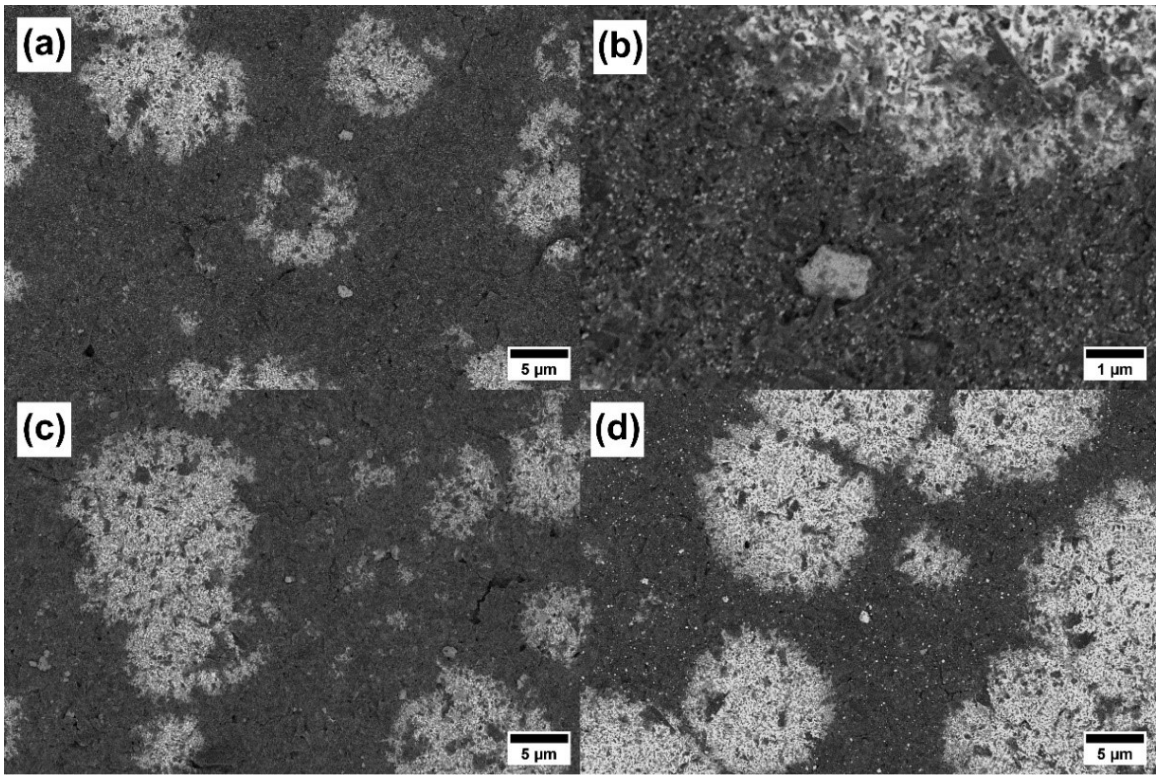

Figure 6. Top-view SEM images of cells taken with T1 detector; (a, b) ZrO_2, (c) NiO, (d) nWO_3.

As shown in Figure 6a-b, ZrO_2 nanoparticles are distributed within the carbon paste in ZrO_2 electrodes along with bigger aggregations of ZrO_2. In NiO electrodes with no ZrO_2, only large

particles were present (Figure 6c). The estimated size of NiO particles from the images was 1-1.5 µm. In Figure 6d it can be seen that for the electrodes with only nanoparticles of WO_3, there were both small and large particles within the carbon ranging from 70 nm to 1.2 µm. The specification of the purchased powder states that particle size is <100 nm, therefore there was also some agglomeration of WO_3 nanoparticles during the fabrication process of the electrodes. Agglomeration of nanosized WO_3 was present in ZrO_2 + nWO_3 cells as well, as seen in Figure 7a. The sizes of WO_3 domains estimated from the image ranged from 100 to 400 nm. The aggregations of nanoparticles resulted in ZrO_2 + nWO_3 electrodes being quite similar to ZrO_2 + WO_3 cells (Figure 7b). For WO_3 powders the size of particles was not specified. However, from the SEM images their size was estimated to be 300-400 nm.

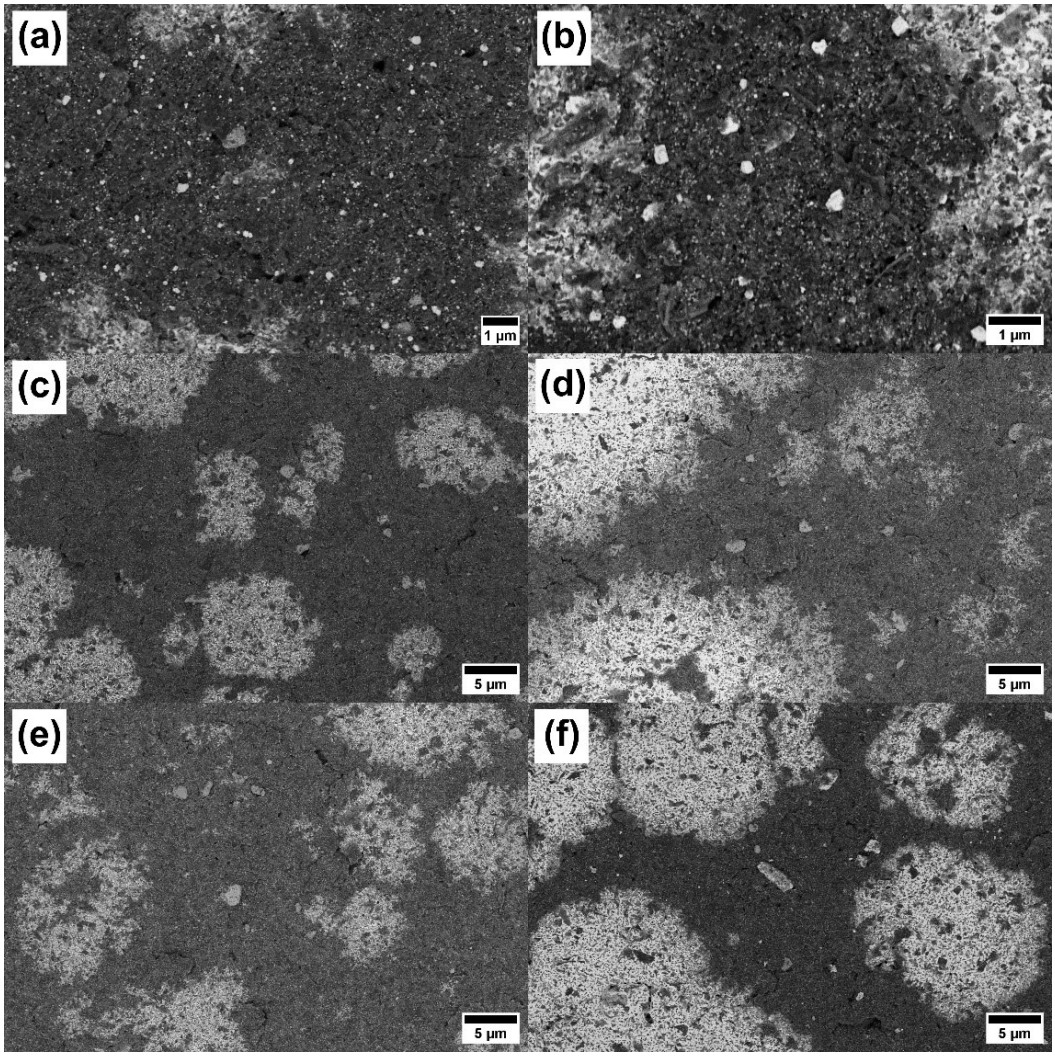

Figure 7. Top-view SEM images of (a) ZrO_2 + nWO_3, (b) ZrO_2 + WO_3, (c) ZrO_2 + CuO, (d) ZrO_2 + MoO_2, (e) ZrO_2 + NiO, (f) ZrO_2 + WO_2 cells.

Cells with ZrO_2 + CuO/MoO_2/NiO/WO_2 all had similar appearances as seen in Figure 7c-f. Oxide domains were distributed across the surface of the electrode. The size of the particles estimated from the SEM images ranged from 1-3 µm.

Top-view EDS analysis was performed to analyse the elemental composition of fabricated C-PSCs. The results of top electrode compositions are presented in Table 4. For all of the samples with ZrO_2, Zr content was 0.8-0.9 at%. For the cells with additional oxides the content of the corresponding element was below 1 at%. EDS analysis confirmed the presence of inorganic binders throughout the surface of prepared carbon electrodes.

Table 4. Elemental composition of prepared electrodes obtained from EDS analysis.

Electrode	C [at%]	Pb [at%]	I [at%]	Zr [at%]	Additional Oxide [at%]
ZrO_2	95.9	0.7	2.6	0.8	-
ZrO_2 + CuO	94.3	0.9	3.4	0.8	0.6 Cu
ZrO_2 + MoO_2	95.0	0.9	2.7	0.9	0.5 Mo
NiO	95.9	0.8	2.7	-	0.6 Ni
ZrO_2 + NiO	92.9	1.3	4.7	0.8	0.3 Ni
ZrO_2 + WO_2	92.9	1.3	4.8	0.8	0.2 W
nWO_3	95.0	1.0	3.5	-	0.4 W
ZrO_2 + nWO_3	95.3	0.8	2.7	0.8	0.4 W
ZrO_2 + WO_3	96.0	0.7	2.0	0.8	0.8 W

5.2 Photovoltaic performance

The performance of devices with fabricated carbon electrodes was evaluated by measuring J-V curves under illumination equivalent to 1 sun. The values of J_{sc}, V_{oc}, fill factor (FF), and PCE were obtained from analysing the recorded JV curves. Shunt electrodes were omitted from the results. The box chart of the reverse scan efficiencies of non-shunt devices is presented in Figure 8.

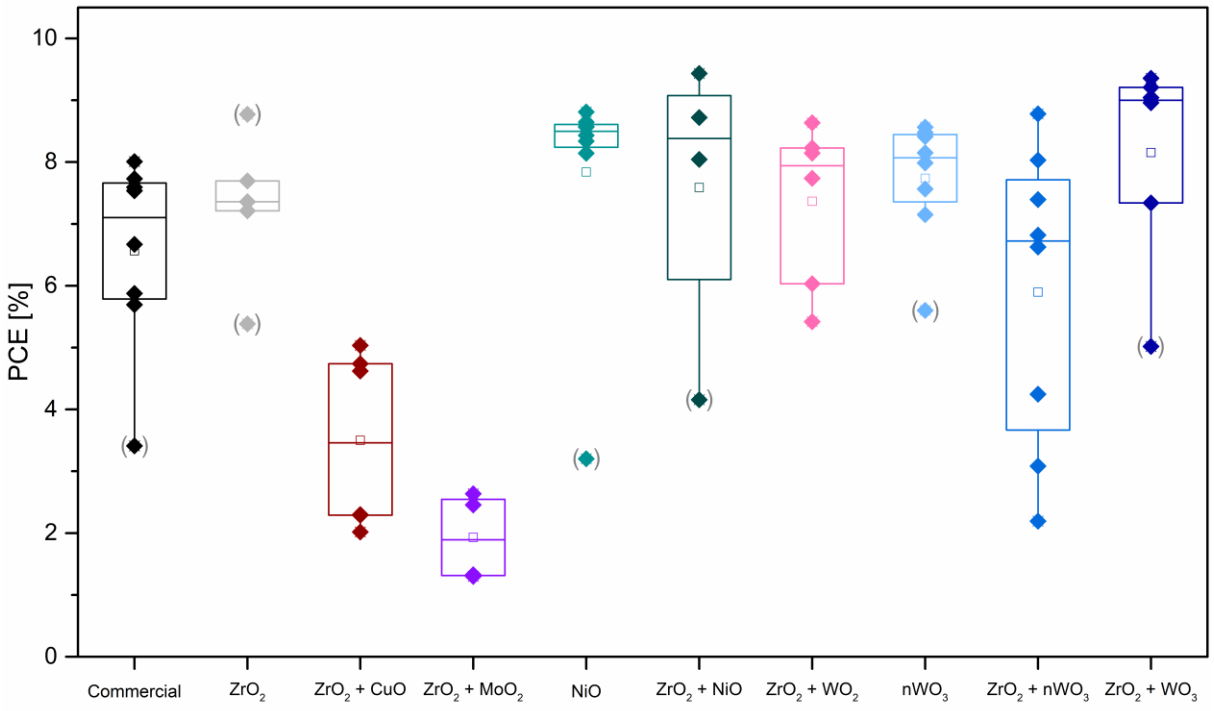

Figure 8. Box charts of PCEs of fabricated cells. The box is formed by 25th (bottom line) and 75th (top line) percentile, mean value is represented by a square, median value is a line inside the box. Lines outside the box (whiskers) extend to 5th (bottom) and 95th (top) percentile. The parentheses on the data points indicate outliers that were excluded from further analysis.

As seen in Figure 8, there were several outliers in the results that could be attributed to inconsistencies during the fabrication process. To get a more accurate overview of performance characteristics, outliers were omitted from the calculations (marked with parentheses in Figure 8). The photovoltaic parameters corresponding to PCE outliers were removed from analysis as well. The average performance characteristics of cells are summarized in Table 5. Devices with ZrO_2 + WO_3 showed the highest PCE of 8.8 ± 0.8%, followed closely by cells with ZrO_2 and NiO incorporations with PCE of 8.7 ± 0.7%. The J-V curve of the champion ZrO_2 + WO_3 cell is shown in Figure 9. Devices with NiO instead of ZrO_2 showed the most reproducible results with a slightly lower efficiency of 8.5 ± 0.2%. Cells with nanosized WO_3 instead of ZrO_2 showed higher average efficiency than devices where both nanosized WO_3 and ZrO_2 where incorporated, with PCE of 8.0 ± 0.5% and 6 ± 2%, respectively. Commercial electrodes had PCE of 7.0 ± 0.9%. Devices with CuO and MoO_2 had the poorest average efficiency of 4 ± 1% and 1.9 ± 0.7%, respectively. Previous studies confirmed the presence of Cu in the absorber layer of cells with CuO-doped electrodes, suggesting that CuO may interact with the perovskite, resulting in decreased performance [14]. Devices with MoO_2 had the lowest J_{sc} among the prepared devices (Table 5), which may

indicate poor filling of the precursor within the mesoporous scaffold. Assuming MoO_2 oxidised to MoO_3 during the sintering of carbon electrodes, results are in accordance with previous research showing poor infiltration of perovskite in cells with MoO_3-doped electrodes [14].

Table 5. Reverse scan J-V characteristics of cells with doped electrodes (outliers omitted).

Name	PCE [%]	J_{sc} [mA/cm^2]	V_{oc} [V]	FF
Commercial	7.0 ± 0.9	17 ± 3	0.81 ± 0.01	0.51 ± 0.05
ZrO_2	7.4 ± 0.2	15 ± 0.5	0.80 ± 0.03	0.60 ± 0.02
ZrO_2 + CuO	4 ± 1	10.3 ± 0.4	0.69 ± 0.08	0.5 ± 0.1
ZrO_2 + MoO_2	1.9 ± 0.7	4 ± 1	0.56 ± 0.04	0.75 ± 0.09
NiO	8.5 ± 0.2	15 ± 1	0.84 ± 0.01	0.66 ± 0.05
ZrO_2 + NiO	8.7 ± 0.7	15.5 ± 0.1	0.84 ± 0.01	0.67 ± 0.05
ZrO_2 + WO_2	7 ± 1	14.8 ± 0.8	0.81 ± 0.05	0.61 ± 0.06
nWO_3	8.0 ± 0.5	15 ± 1	0.81 ± 0.03	0.68 ± 0.04
ZrO_2 + nWO_3	6 ± 2	14 ± 2	0.7 ± 0.1	0.6 ± 0.1
ZrO_2 + WO_3	8.8 ± 0.8	15.9 ± 0.7	0.83 ± 0.02	0.67 ± 0.05

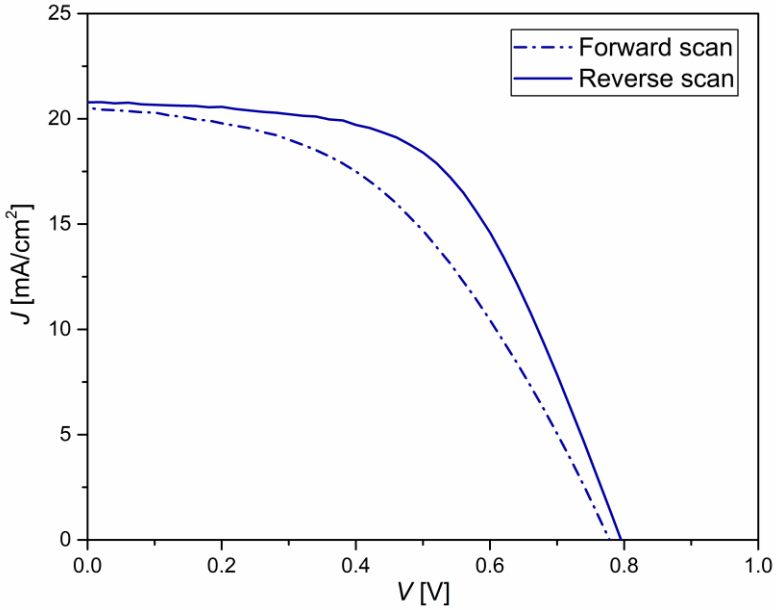

Figure 9. J-V curve of the champion ZrO_2 + WO_3 device, measured with a scan rate of 100 mV/s.

The values of J_{sc} for all cells are shown in Figure 10. Commercial electrodes had the highest J_{sc} of 17 ± 3 mA/cm^2 despite a large variation across the samples. Fabricated electrodes had more reproducible J_{sc} values across samples, but the average current density was lower than

that of the commercial samples. As it can be seen from Figure 10, some cells with nanoparticles of WO_3 still had irregularities in recorded J_{sc} values. This could be attributed to the differences in infiltration due to the agglomerations of particles observed in the SEM images (Figure 6d and Figure 7a).

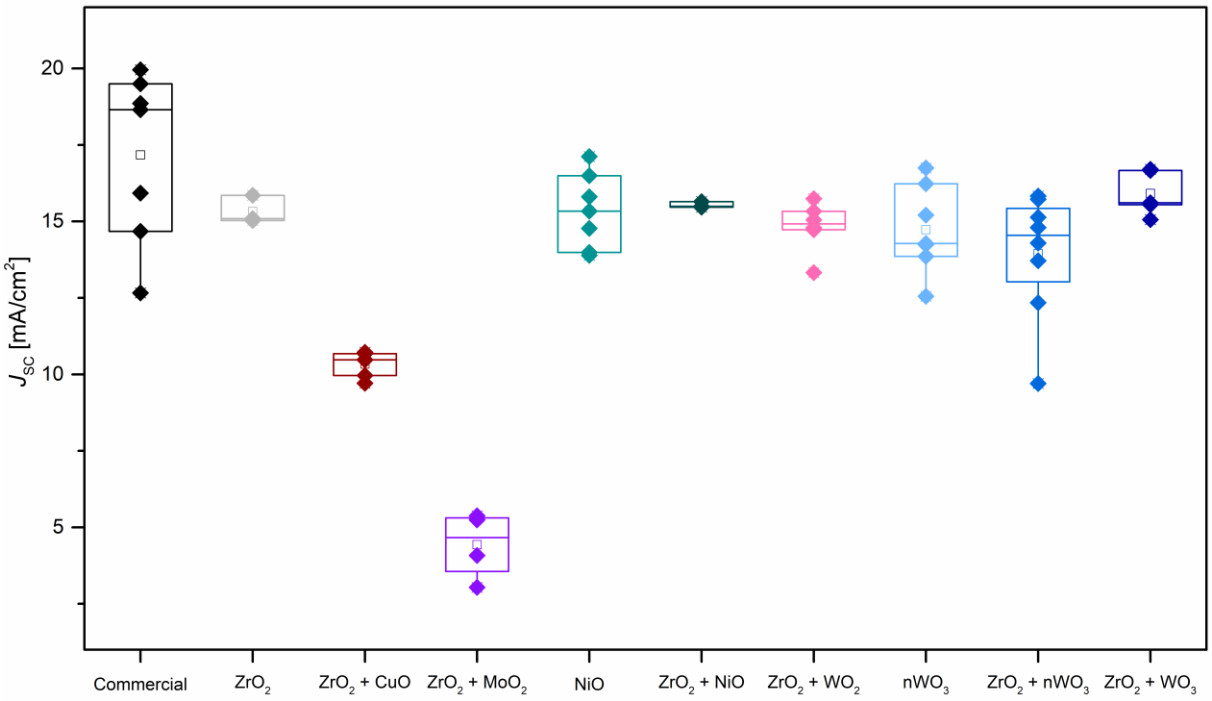

Figure 10. J_{sc} values of fabricated cells. The box is formed by 25th (bottom line) and 75th (top line) percentile, mean value is represented by a square, median value is a line inside the box. Lines outside the box (whiskers) extend to 5th (bottom) and 95th (top) percentile. The characteristics corresponding to PCE outliers were omitted.

The incorporation of hole transport materials should result in higher V_{oc} values for fabricated devices due to better energy alignment. As shown in Table 5 and Figure 11, devices with NiO, WO_2, WO_3 had higher V_{oc} compared to ZrO_2 devices. Devices with nWO_3 had the slightly average V_{oc} of 0.81 ± 0.03 V than ZrO_2 cells, while ZrO_2 + nWO_3 had a lower average V_{oc} value equal to 0.7 ± 0.1 V due to large variations in V_{oc} across the samples. For all the fabricated electrodes V_{oc} values were less reproducible compared to J_{sc}, and appear to be the reason for outlier PCE values. Changes in V_{oc} could occur due to charge recombination at the carbon electrode interface. In this case, the increase in recombination could have happened due to inconsistences during the electrode manufacturing process. Doctor-blading was done manually, therefore there was some variability in electrode thickness and area. In the future works, this could be remedies by using automated screen-printing technique for the fabrication of carbon electrodes.

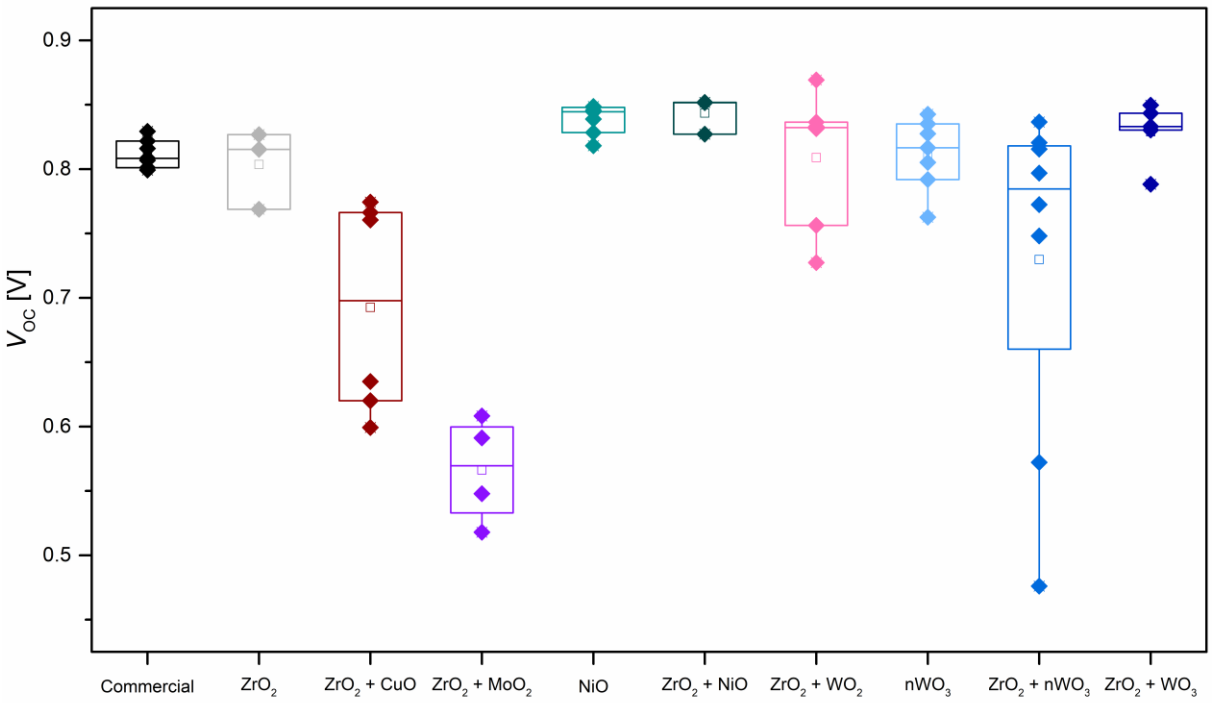

Figure 11. V_{oc} values of fabricated devices. The box is formed by 25th (bottom line) and 75th (top line) percentile, mean value is represented by a square, median value is a line inside the box. Lines outside the box (whiskers) extend to 5th (bottom) and 95th (top) percentile. The characteristics corresponding to PCE outliers were omitted.

Figure 12 shows the obtained FF values of fabricated devices. FF is a parameter found by dividing the power at maximum power point of JV curve by V_{oc} and J_{sc} of the cell. FF can serve as an indicator of the charge extraction efficiency and point to recombination losses within the cell. Cells with MoO_2 additions had the highest FF of 0.75 ± 0.09 due to low performance characteristics resulting in inflated FF values. ZrO_2 and nWO_3 electrodes FF values were equal to 0.6. As seen in Figure 12, devices with NiO, WO_2, WO_3 additions had higher values of FF than electrodes with only ZrO_2, pointing to more efficient charge extraction processes within the cells. Interestingly, despite having high J_{SC} and V_{OC} characteristics, commercial electrodes had lower FF than fabricated electrodes (aside from ZrO_2 + CuO). This highlights the importance of optimising the carbon paste formulation to achieve higher efficiencies of C-PSCs.

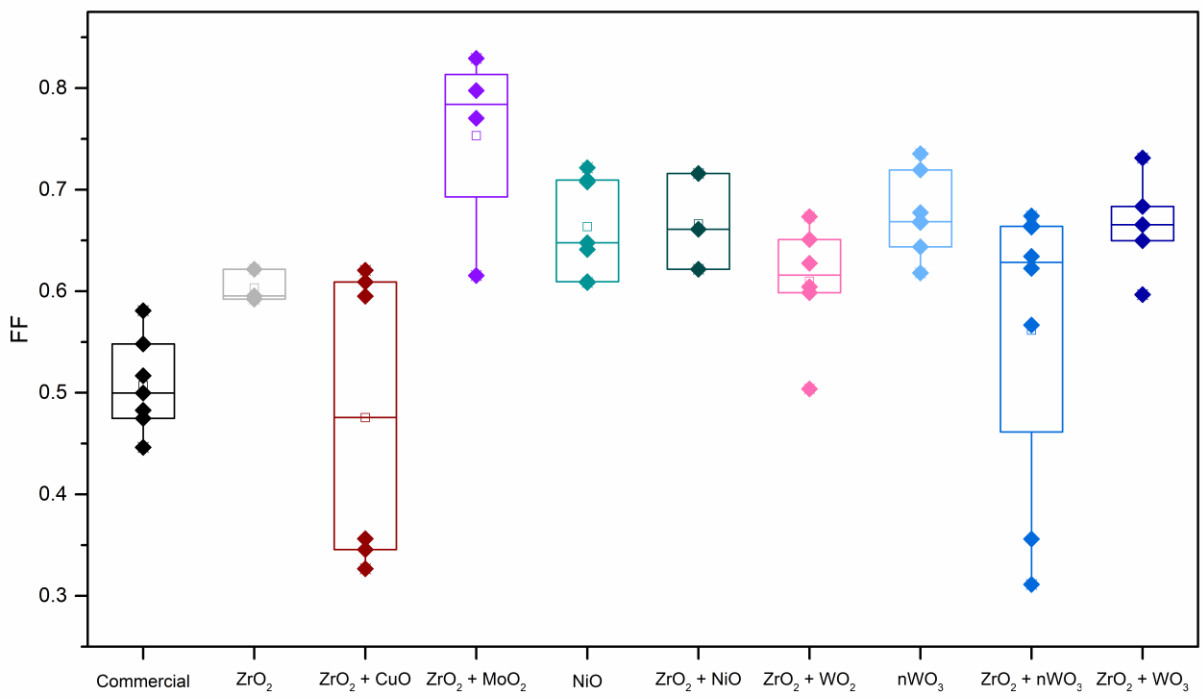

Figure 12. FF values of fabricated cells (PCE outliers omitted). The box is formed by 25th (bottom line) and 75th (top line) percentile, mean value is represented by a square, median value is a line inside the box. Lines outside the box (whiskers) extend to 5th (bottom) and 95th (top) percentile. The characteristics corresponding to PCE outliers were omitted.

Maximum power point (MPP) tracking was used to study the reliability of the fabricated devices' performance. MPP tracking measurement was done for 300 seconds under 1 sun illumination. As shown in Figure 13, in the first seconds the power output peaks and then reaches a stable value. All devices exhibited stable performance at MPP over 5 minutes. Device with ZrO_2 + MoO_2 additions had a low power output due to low performance characteristics as was shown in Table 5.

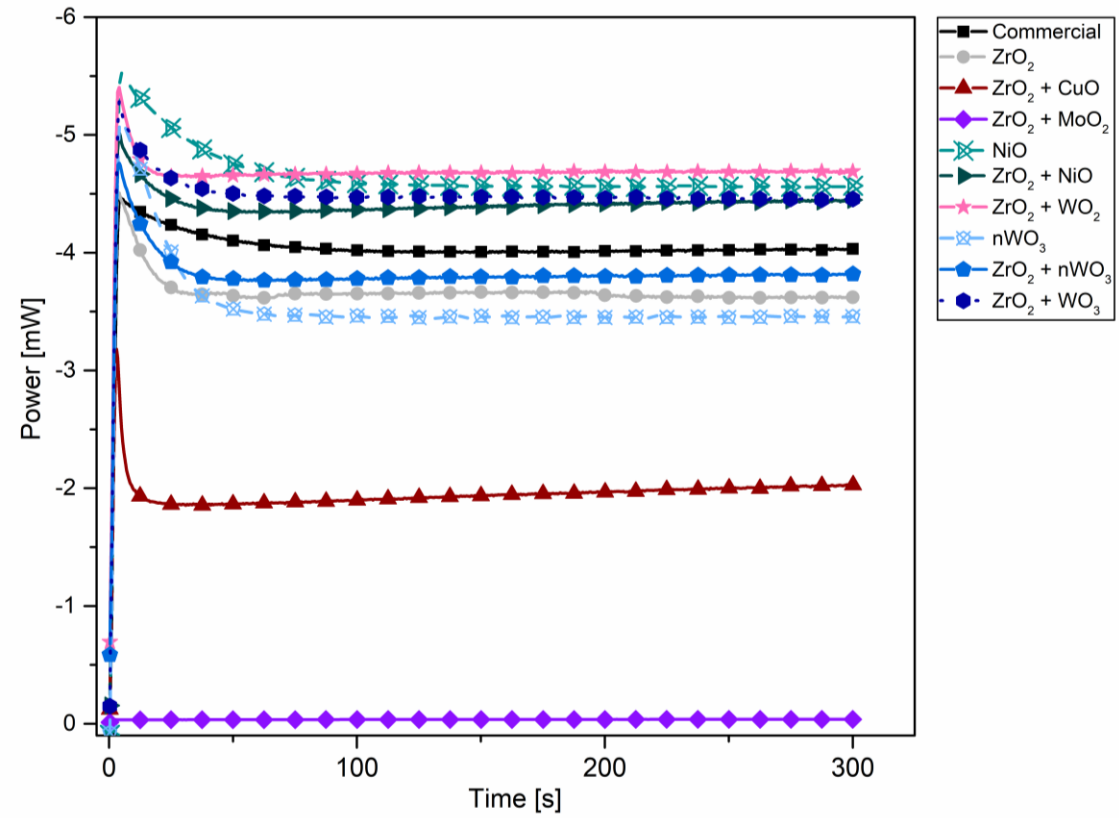

Figure 13. MPP tracking of fabricated devices over 300 seconds. Champion devices of batch 1 were chosen for the analysis. Symbols represent every 25 recorded values.

5.3 Electrochemical impedance spectroscopy measurements

Electrochemical impedance spectroscopy (EIS) was performed to investigate the differences in resistances of devices with manufactured carbon electrodes. EIS was performed under 1 sun illumination at open circuit voltage. Impedance results were fitted to the equivalent circuit (Figure 5) to obtain quantitative data of the resistances within the devices. Nyquist plots of the recorded EIS spectra for the fabricated devices are shown in Figure 14. For all cells three-feature spectra was observed with three semicircles.

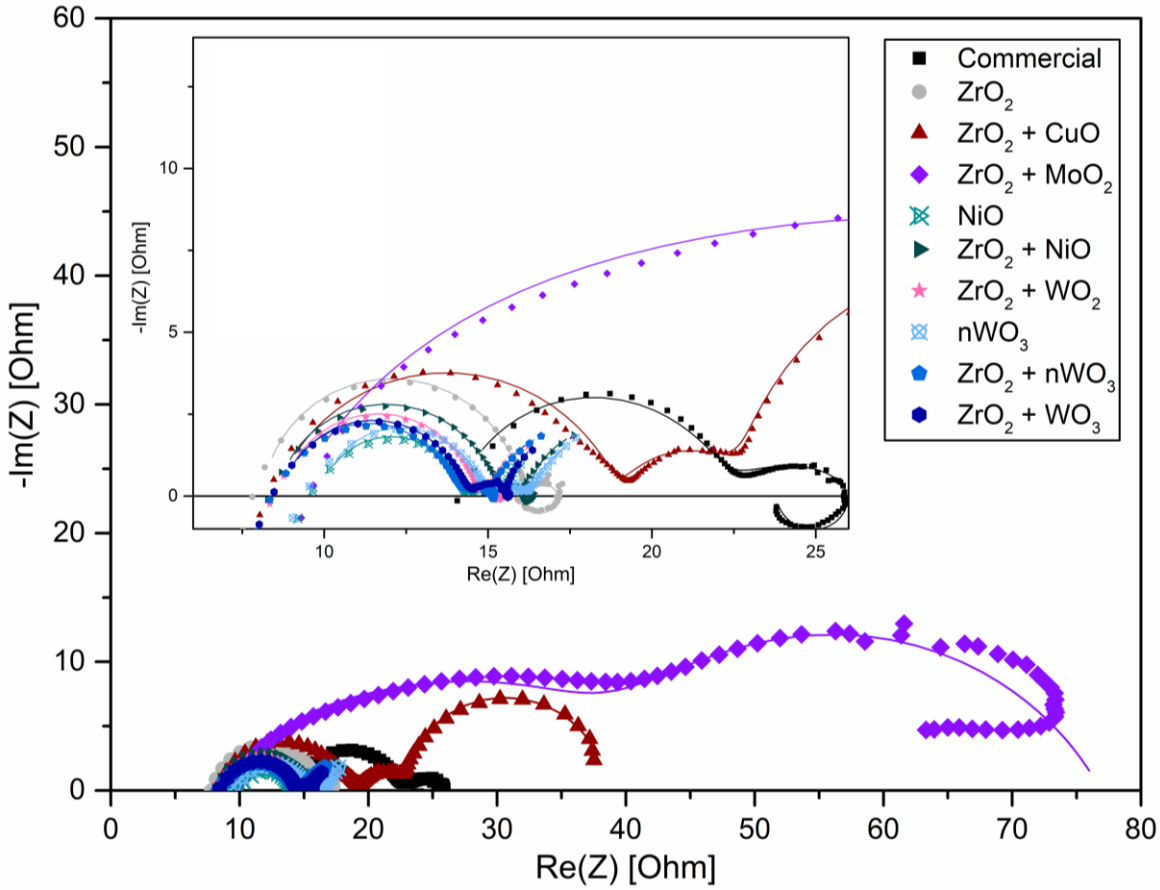

Figure 14. Nyquist plots for fabricated devices; inset shows a close-up of the spectra in the high-frequency region. Champion devices from batch 3 were chosen for analysis. Solid lines correspond to fits using the equivalent circuit shown in Figure 5.

From the fitted results we can obtain the values for series resistance R_s, related to the sheet resistances of FTO and carbon electrodes, represented as the offset of the EIS spectra from the origin. The semicircle in high-frequency (HF) region is related to the hole transport process from the absorber to the carbon electrode [96]. Its diameter gives the values of the charge-transfer resistance R_{HF}. The values of R_s and R_{HF} calculated from the fits are shown in Table 6.

Table 6. Fitted resistance values of champion devices per each studied condition, normalized by the aperture area of 0.64 cm^2.

Name	R_s [Ohm/cm^2]	R_{HF} [Ohm/cm^2]	R_{MF} [Ohm/cm^2]	R_{LF} [Ohm/cm^2]
Commercial	21.9	12.5	7.2	-4.4
ZrO_2	12.7	12.3	2.2	-2.1
ZrO_2 + CuO	13.2	16.4	6.1	24.6
ZrO_2 + MoO_2	14.1	21.8	22.9	61.4
NiO	15.4	6.7	2.2	7.0
ZrO_2 + NiO	13.3	10.0	2.0	7.6
ZrO_2 + WO_2	13.6	9.2	1.1	5.7
nWO_3	14.7	6.9	5.1	9.4
ZrO_2 + nWO_3	13.6	8.2	2.0	7.3
ZrO_2 + WO_3	13.6	8.7	2.2	6.3

As it can be seen from the results shown in Table 6, the series resistances for prepared carbon pastes had quite close values. R_s of the ZrO_2 device was the lowest among the fabricated pastes (12.7 Ohm/cm^2), and a slight increase was observed for other fabricated electrodes. Fitted R_s values mostly corroborate the mean sheet resistance values shown in Table 3. Slight inconsistencies between mean sheet resistance and obtained R_s values could be attributed to batch-to-batch variations of the fabricated electrodes. Commercial electrode R_s was higher than the values for prepared pastes. This may indicate that the composition of the commercial carbon paste had different types and ratios of constituents that increased the sheet resistance of the electrode.

The values of R_{HF} give insights into the charge-transfer resistance of the carbon electrodes. Commercial and ZrO_2 electrodes had similar R_{HF} of 12.5 and 12.3 Ohm/cm^2, respectively. Replacing ZrO_2 with NiO had the highest impact on the charge-transfer, decreasing it to 6.7 Ohm/cm^2. NiO additions can effectively adjust the work function of carbon electrode, thus improving the hole transport from the perovskite to carbon [78]. Similarly, cells with only nanosized WO_3 had a lower R_{HF} of 6.9 Ohm/cm^2. WO_3 nanoparticles have been previously used to improve the performance of C-PSCs through improved hole extraction [18,19]. Based on the fitted results in Table 6 replacing ZrO_2 with a semiconducting oxide can improve the charge transport of the carbon electrodes. The combination of ZrO_2 and NiO had R_{HF} of 10.0 Ohm/cm^2, while cells with a combination of ZrO_2 and WO_x additions had lower R_{HF} values than cells with ZrO_2. This points to an enhanced hole extraction within the carbon electrodes

due to inclusion of HTL oxides. ZrO_2 + CuO and ZrO_2 + MoO_2 cells had R_{HF} values of 16.4 and 21.8 Ohm/cm^2, respectively, indicating a more inhibited charge transfer, in accordance with the PCE results presented in Table 5.

Low-frequency (LF) semicircle in the Nyquist plot has been associated with charge recombination in HTL-free mp-PSCs [96]. However, in this case instead of one semicircle, two features have been observed (Figure 14). Previous reports have associated medium-frequency (MF) and LF semicircles with iodide ion vacancy migration within the cells [91]. The fitted resistance values of R_{MF} and R_{LF} are shown in Table 6. Among the recorded spectra there were both negative and positive LF features. The sign of the LF feature is determined by the nature of recombination – it can be either electron- or hole-limited [91]. For spectra with a positive LF semicircle, Nyquist plots of some samples exhibited small loop artifacts connecting the MF and LF semicircles. Loops have been connected to the drift of ionic species and their effect on the trap states [89,92]. On the other hand, the presence of loops could also be associated with instabilities occurring within the cells during a prolonged EIS measurement [97].

Most of the literature on EIS analysis of PSCs focuses on devices with conventional structure that includes both electron and hole transport layers [91,92]. The literature on the EIS studies of HTL-free mp-PSCs is limited due to the unique structure of devices and mostly focuses on two-feature spectra [96,98]. Therefore, it is difficult to confidently assign physical phenomena to the features observed in the MF and LF regions of the recorded EIS spectra.

5.4 Stability test

The stability of fabricated devices was investigated in a dark storage test at room temperature (T = 25 °C) under high humidity conditions (RH = 85%). Devices were stored without encapsulation. The results of stability test over 500 hours are presented in Figure 15.

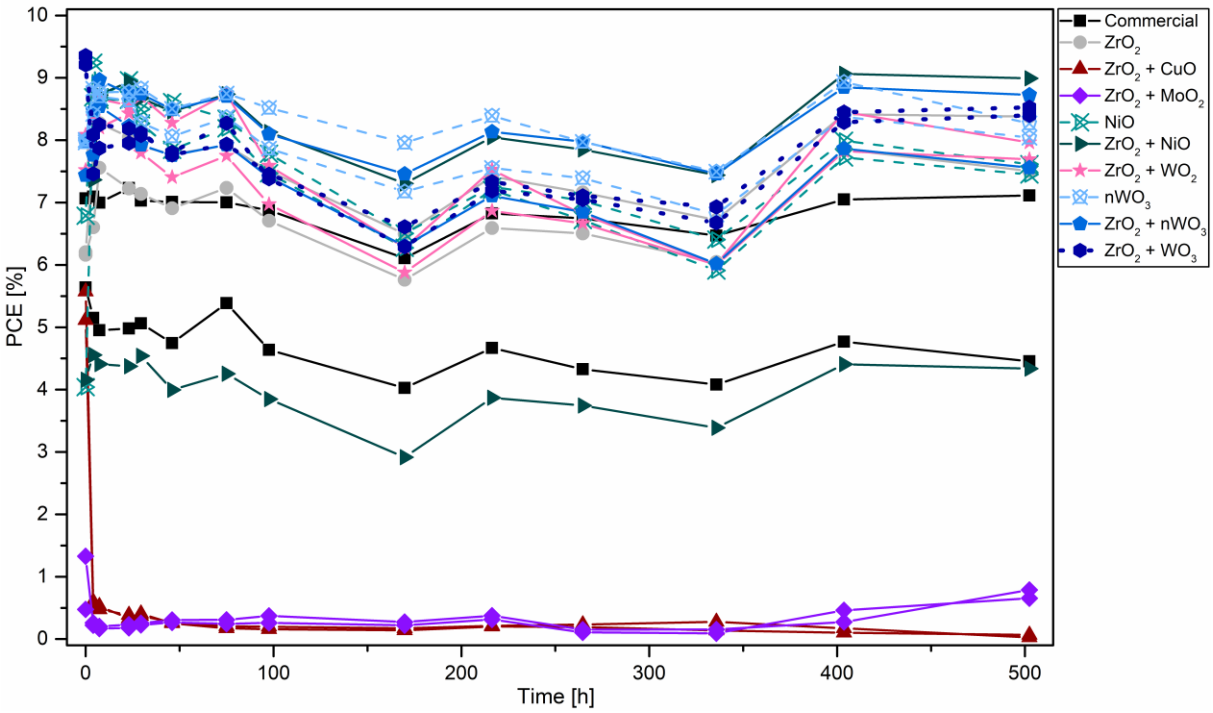

Figure 15. Stability test of cells under dark storage, RH = 85%, *T* = 25 °C for 500 hours.

As it can be seen in Figure 15, most of the cells maintained their efficiencies under high-humidity conditions for over 500 hours. An increase in PCE was observed for most of the fabricated cells in the first 8 hours of the experiment. It could be attributed to the stabilisation of the devices in the ambient air and moisture after being stored in a N_2-filled glovebox prior to the experiment. After the initial stabilisation, cells with ZrO_2, NiO, WO_2, and WO_3 inclusions exhibited good performance over the course of the experiment. Despite observed fluctuations in PCE throughout the test, after 500 hours cells retained >90% of their initial efficiency.

On the other hand, the efficiency of devices with ZrO_2 + CuO electrodes sharply decreased after only 4 hours of storage under high-humidity conditions. Previous research shows that Cu and CuO can migrate into the perovskite layer [14]. There, CuO may react with decomposition products of the perovskite, accelerating the degradation of the absorber layer [99]. Devices with ZrO_2 + MoO_2 additions degraded quickly as well, indicating that MoO_2 additions to the carbon electrode offer poor protection of the perovskite absorber from the environmental factors.

The degradation of the perovskite could be observed through the change of the cell color, as seen in Figure 16. The shift from black to yellow signifies the degradation of the perovskite

absorber and the formation of lead iodide [100]. Devices with ZrO_2 + WO_3 (Figure 16a-c) remained black after storage for 500 hours in high-humidity conditions, indicating good stability of the C-PSC. Devices with ZrO_2 + CuO additions turned from black at the beginning of the test (Figure 16d) to yellow. The degradation was first observed around the edges (Figure 16e), and then it spread across the cell (Figure 16f).

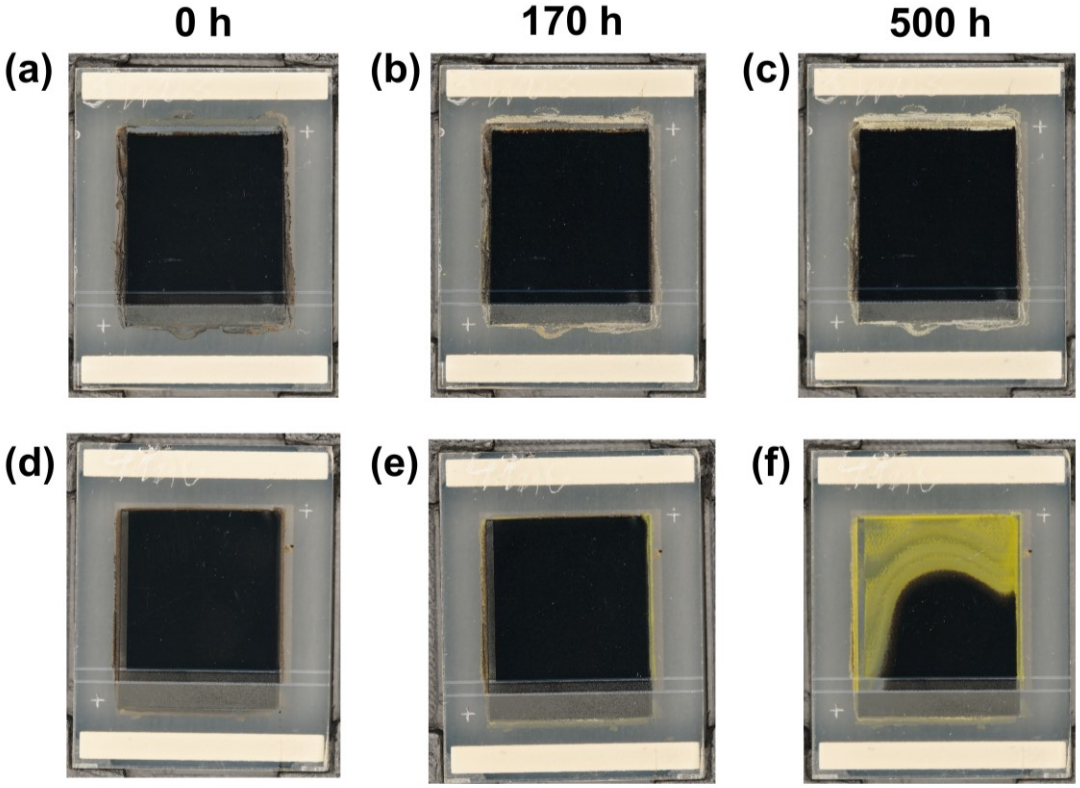

Figure 16. Photos taken throughout the stability test of the ZrO_2 + WO_3 device at (a) 0 hours, (b) 170 hours, (c) 500 hours, and ZrO_2 + CuO device at (d) 0 hours, (e) 170 hours, (f) 500 hours.

5.5 Revival

Fabricated devices were remanufactured by a revival treatment employing GVL as solvent for washing out the perovskite. The performance of revived devices was measured and compared to the initial characteristics. Revival rate was defined as the ratio of revived PCE to initial PCE. Calculated revival rates for fabricated electrodes are presented in Figure 17.

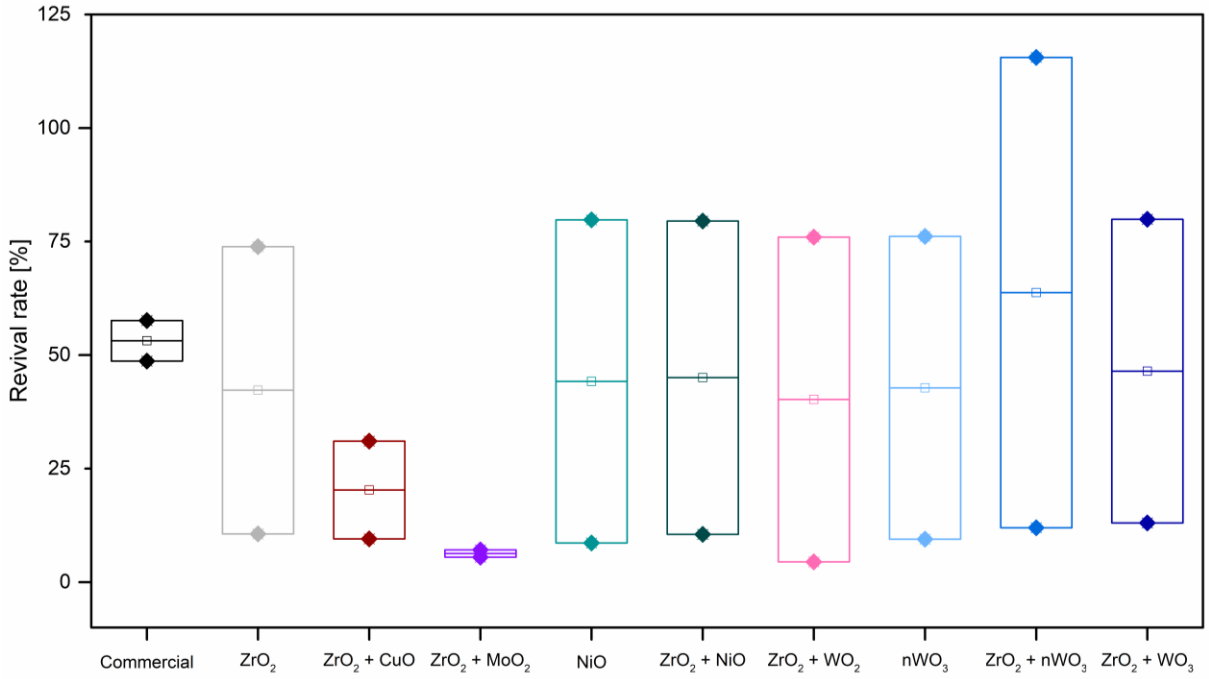

Figure 17. Revival rates of fabricated devices. The box is formed by 25th (bottom line) and 75th (top line) percentile, mean value is represented by a square, median value is a line inside the box. Lines outside the box (whiskers) extend to 5th (bottom) and 95th (top) percentile.

After the revival process, ZrO_2 + MoO_2 cells showed signs of swelling and detachment of carbon electrode from the stack. This could indicate that MoO_2 affected the porosity of the carbon electrode, which in turn affects the degree of infiltration of perovskite precursor within the device scaffold [74]. Poor infiltration leads to incomplete filling of mesopores, resulting in low efficiencies and decreased revival rates. Flaking and peeling of the commercial electrodes was observed, suggesting that the commercial paste is not robust enough to withstand the revival process. The rest of the fabricated electrodes retained their structural integrity, suggesting a good adhesion of the carbon paste to the substrate.

As it can be seen, there was quite a large discrepancy between the revival rates per electrode sample for several cells. However, the difference seems to occur due to the quality of the solvent used for the revival, rather due to the electrodes themselves. GVL used in the experiment came from different batches – old batch was ordered approximately 6 months before the experiment, and a new batch was ordered one month before the experiment. The difference was apparent during the washing out of the perovskite. After dissolution of $MAPbI_3$ old solvent changed colour from transparent to light yellow, while the newer GVL turned to a bright yellow-orange colour. If we plot the revival rates based on the solvent

batch, we can see that the revival rates are quite close to each other (Figure 18). The average revival rate for cells revived with new and old GVL was 18% and 83%, respectively.

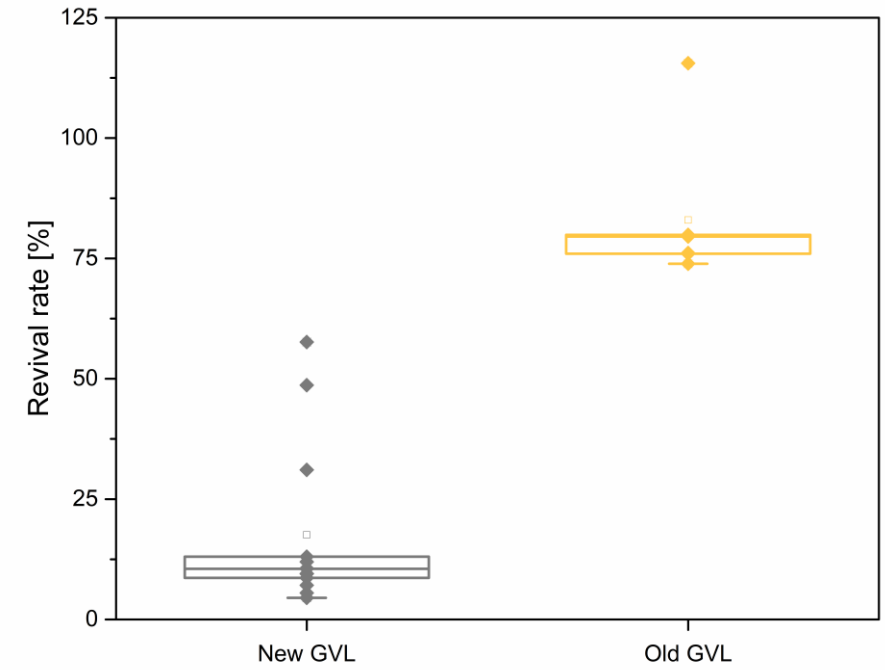

Figure 18. Revival rates based on GVL age. The box is formed by 25th (bottom line) and 75th (top line) percentile, mean value is represented by a square, median value is a line inside the box. Lines outside the box (whiskers) extend to 5th (bottom) and 95th (top) percentile.

The hypothesis is that the purity and viscosity of the solvent changes from batch to batch, affecting how well the solvent residue is removed from within the mesoporous stack. This, in turn, influences the re-infiltration of the perovskite precursor solution. Revived devices with poor perovskite filling show low PCEs, resulting in low revival rates. The difference is noticeable from the appearance of the revived devices (Figure 19). Cells with good perovskite infiltration turn black, while devices with incomplete pore filling and poor perovskite crystallisation remain a grey colour.

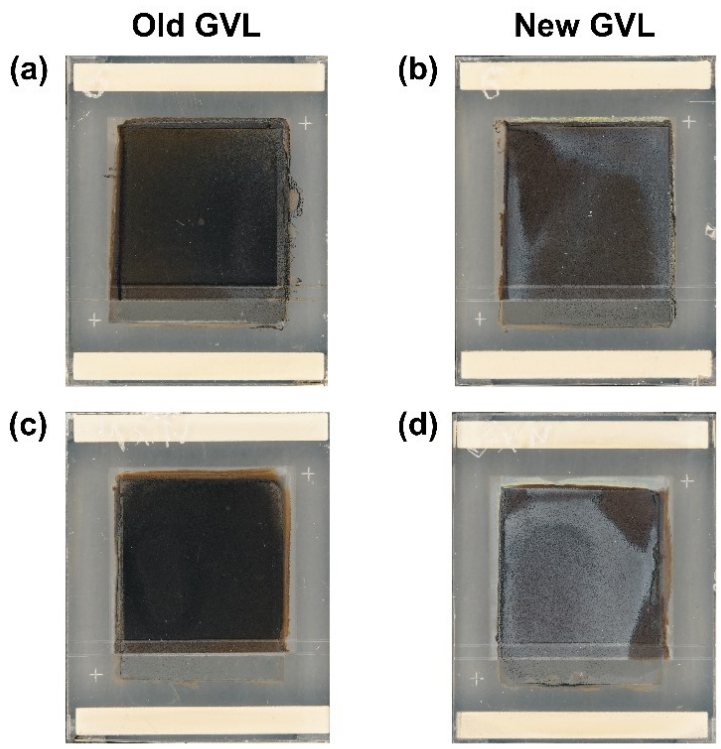

Figure 19. Pictures of cells revived with (a,c) old and (b,d) new GVL.

The results suggest that the revival protocol needs to be further optimized to obtain reproducible results. It might be necessary to adjust the GVL viscosity by mixing it with other solvent (e.g., ethanol) or modify the ethanol washing step to ensure complete removal of GVL from within the cell stack.

6 Conclusions

This thesis aimed to explore the effect of different carbon electrode compositions on performance, stability, and revival rate of HTL-free C-PSCs. The composition of carbon paste was varied by modifying the inorganic oxide binder component of the paste. Various oxides were used, such as ZrO_2, NiO, and WO_3, as well as combinations of ZrO_2 and CuO, MoO_2, NiO, WO_2, and WO_3.

The mean sheet resistance of fabricated electrode films was measured using a four-point probe technique. The obtained values showed small differences between the fabricated films. Despite metallic conductivity of MoO_2, its addition did not decrease the mean sheet resistance of the carbon paste. This is hypothesised to occur due to oxidation of MoO_2 to MoO_3 during the sintering process. The morphology of the electrodes on top of fabricated devices was investigated using SEM. Images showed even distribution of oxide particles on the surface of the electrodes. The size of CuO, MoO_2, NiO, and WO_2 particles was estimated to be 1-3 µm. Cells with nanosized particles of WO_3 showed agglomerations in the <1 µm range. EDS was used to analyse the top-view elemental composition of the electrodes, confirming the presence of evenly distributed oxides on the surface of the electrodes.

The performance of devices was studied using J-V curves recorded under 1 sun illumination. The best performance was achieved for devices with a combination of ZrO_2 and WO_3 that showed the highest average PCE of 8.7%, and cells with a mix of ZrO_2 and NiO exhibiting average PCE of 8.5%. The addition of CuO and MoO_2 to the carbon paste had a detrimental effect on the performance of devices. The results were in accordance with previous reports showing that CuO can interact with the perovskite absorber, leading to poor device performance. Poor PCE of ZrO_2 and MoO_2 can be attributed to poor infiltration of the perovskite precursor. Moreover, MPP tracking was used to study the short-term operational stability of fabricated cells. All devices exhibited stable performance over 5 minutes of stressing under illumination.

Furthermore, EIS was utilized to study the effect of oxides on the resistances within the perovskite solar cells. The obtained data was fitted to an equivalent circuit to obtain quantitative values of resistances. The fitted R_s values for fabricated carbon electrodes were close to each other. The fitted R_{HF} values represented the charge-transfer resistance of the

carbon electrode. The results showed that the charge transport of the carbon electrodes improved when ZrO_2 was replaced with a semiconducting oxide binder. Electrodes with MoO_2 and CuO additions had the highest R_{HF} values, corroborating the observed poor photovoltaic performance.

The dark storage stability of the cells was evaluated in an aging test with RH of 85%. It was found that cells with MoO_2 and CuO additions immediately degraded after being exposed to a high-humidity environment. The rest of the cells with fabricated carbon electrodes showed good stability, maintaining over 90% of their initial efficiency after 500 hours.

One of the advantages of HTL-free C-PSCs is the possibility to recycle them through a facile solvent-based revival process. The performance of initial and revived devices was compared after a GVL-based the revival treatment with GVL was applied to fabricated of C-PSCs. After the treatment, devices with MoO_2 additions showed signs of detachment from the substrate, suggesting poor porosity of the electrode and incompatibility with the revival process. The rest of the fabricated electrodes did not show signs of degradation. However, the experiment was affected by the quality of the solvent used. This highlighted the need for further optimisation of the solvent formulation used in the revival protocol.

Overall, this thesis investigated the effect of the inorganic oxide additives of the carbon paste on the photovoltaic performance, and stability, and revival of HTL-free C-PSCs. The results indicate that the choice of inorganic additives plays a key role in determining the overall device performance, lifetime, and revival in HTL-free C-PSCs. Further work could build upon the obtained results and focus on the optimisation of the constituents of carbon paste or other layers of HTL-free C-PSCs.

References

[1] K. Calvin, D. Dasgupta, G. Krinner, A. Mukherji, P.W. Thorne, C. Trisos, J. Romero, P. Aldunce, K. Barrett, G. Blanco, W.W.L. Cheung, S. Connors, F. Denton, A. Diongue-Niang, D. Dodman, M. Garschagen, O. Geden, B. Hayward, C. Jones, F. Jotzo, T. Krug, R. Lasco, Y.-Y. Lee, V. Masson-Delmotte, M. Meinshausen, K. Mintenbeck, A. Mokssit, F.E.L. Otto, M. Pathak, A. Pirani, E. Poloczanska, H.-O. Pörtner, A. Revi, D.C. Roberts, J. Roy, A.C. Ruane, J. Skea, P.R. Shukla, R. Slade, A. Slangen, Y. Sokona, A.A. Sörensson, M. Tignor, D. Van Vuuren, Y.-M. Wei, H. Winkler, P. Zhai, Z. Zommers, J.-C. Hourcade, F.X. Johnson, S. Pachauri, N.P. Simpson, C. Singh, A. Thomas, E. Totin, A. Alegría, K. Armour, B. Bednar-Friedl, K. Blok, G. Cissé, F. Dentener, S. Eriksen, E. Fischer, G. Garner, C. Guivarch, M. Haasnoot, G. Hansen, M. Hauser, E. Hawkins, T. Hermans, R. Kopp, N. Leprince-Ringuet, J. Lewis, D. Ley, C. Ludden, L. Niamir, Z. Nicholls, S. Some, S. Szopa, B. Trewin, K.-I. Van Der Wijst, G. Winter, M. Witting, A. Birt, M. Ha, IPCC, 2023: Climate Change 2023: Synthesis Report. Contribution of Working Groups I, II and III to the Sixth Assessment Report of the Intergovernmental Panel on Climate Change [Core Writing Team, H. Lee and J. Romero (eds.)]. IPCC, Geneva, Switzerland., First, Intergovernmental Panel on Climate Change (IPCC), 2023. https://doi.org/10.59327/IPCC/AR6-9789291691647.

[2] Paris Agreement to the United Nations Framework Convention on Climate Change, (2015).

[3] IRENA, 2024 Year in Review: Climate-driven Global Renewable Energy Resources and Energy Demand, (2025).

[4] IEA, Renewables 2025, (2025).

[5] D.S. Philipps, F. Ise, W. Warmuth, P.P. GmbH, Photovoltaics Report, (2025). https://www.ise.fraunhofer.de/en/publications/studies/photovoltaics-report.html (accessed February 17, 2026).

[6] J.C. Blakesley, R.S. Bonilla, M. Freitag, A.M. Ganose, N. Gasparini, P. Kaienburg, G. Koutsourakis, J.D. Major, J. Nelson, N.K. Noel, B. Roose, J.S. Yun, S. Aliwell, P.P. Altermatt, T. Ameri, V. Andrei, A. Armin, D. Bagnis, J. Baker, H. Beath, M. Bellanger, P. Berrouard, J. Blumberger, S.A. Boden, H. Bronstein, M.J. Carnie, C. Case, F.A. Castro, Y.-M. Chang, E. Chao, T.M. Clarke, G. Cooke, P. Docampo, K. Durose, J.R. Durrant,

M.R. Filip, R.H. Friend, J.M. Frost, E.A. Gibson, A.J. Gillett, P. Goddard, S.N. Habisreutinger, M. Heeney, A.D. Hendsbee, L.C. Hirst, M.S. Islam, K.D.G.I. Jayawardena, M.B. Johnston, M. Kauer, J. Kettle, J.-S. Kim, D. Lamb, D. Lidzey, J. Lim, R. MacKenzie, N. Mason, I. McCulloch, K.P. McKenna, S.B. Meier, P. Meredith, G. Morse, J.D. Murphy, C. Nicklin, P. Ortega-Arriaga, T. Osterberg, J.B. Patel, A. Peaker, M. Riede, M. Rush, J.W. Ryan, D.O. Scanlon, P.J. Skabara, F. So, H.J. Snaith, L. Steier, J. Thiesbrummel, A. Troisi, C. Underwood, K. Walzer, T. Watson, J.M. Walls, A. Walsh, L.D. Whalley, B. Winchester, S.D. Stranks, R.L.Z. Hoye, Roadmap on established and emerging photovoltaics for sustainable energy conversion, J. Phys. Energy 6 (2024) 041501. https://doi.org/10.1088/2515-7655/ad7404.

[7] National Laboratory of the Rockies, Golden, CO, NLR Best Research-Cell Efficiency Chart, (n.d.). https://www.nlr.gov/pv/cell-efficiency (accessed February 10, 2026).

[8] M. Afroz, R.K. Ratnesh, S. Srivastava, J. Singh, Perovskite solar cells: Progress, challenges, and future avenues to clean energy, Sol. Energy 287 (2025) 113205. https://doi.org/10.1016/j.solener.2024.113205.

[9] E.S. Akulenko, M. Hadadian, A. Santasalo-Aarnio, K. Miettunen, Eco-design for perovskite solar cells to address future waste challenges and recover valuable materials, Heliyon 9 (2023) e13584. https://doi.org/10.1016/j.heliyon.2023.e13584.

[10] A. Mei, X. Li, L. Liu, Z. Ku, T. Liu, Y. Rong, M. Xu, M. Hu, J. Chen, Y. Yang, M. Grätzel, H. Han, A hole-conductor–free, fully printable mesoscopic perovskite solar cell with high stability, Science 345 (2014) 295–298. https://doi.org/10.1126/science.1254763.

[11] J. Xiang, C. Han, Y. Cheng, Q. Gao, W. Hu, Y. Zhou, A. Mei, Y. Zhou, H. Han, Recent Progress and Advances of Perovskite Crystallization in Carbon-Based Printable Mesoscopic Solar Cells, Adv. Mater. 37 (2025) 2415405. https://doi.org/10.1002/adma.202415405.

[12] T. Binyamin, L. Etgar, Ways to Improve the Performance of Triple-Mesoscopic Hole-Conductor-Free Perovskite-Based Solar Cells, Sol. RRL 6 (2022) 2200295. https://doi.org/10.1002/solr.202200295.

[13] H. Xie, J. Lei, Z. Zhu, X. Xu, D. Li, J. Xu, Y. Pan, X. Yin, Practical Interface Engineering between Perovskite and Carbon Electrode in Regular Carbon-Based Perovskite Solar Cells, ACS Appl. Mater. Interfaces 17 (2025) 33271–33295. https://doi.org/10.1021/acsami.4c20906.

[14] P. Jiang, Y. Xiong, M. Xu, A. Mei, Y. Sheng, L. Hong, T.W. Jones, G.J. Wilson, S. Xiong, D. Li, Y. Hu, Y. Rong, H. Han, The Influence of the Work Function of Hybrid Carbon Electrodes on Printable Mesoscopic Perovskite Solar Cells, J. Phys. Chem. C 122 (2018) 16481–16487. https://doi.org/10.1021/acs.jpcc.8b02163.

[15] S. Nakhaeenejad, M. Shojaeifar, S. Maghsoudi, F. Arjmand, Z. Golshani, Enhancing the efficiency of hole-transport-free perovskite solar cells using nickel oxide nanoparticles as a dopant in graphite-based carbon electrodes, J. Phys. Chem. Solids 189 (2024) 111958. https://doi.org/10.1016/j.jpcs.2024.111958.

[16] W. Zhou, S. Hong, F. Yu, J. Wan, Q. Wang, X. Zhou, Synergy of hybrid carbon electrode and differential pressure driven MAPbI3 crystal growth on the performance of mesoscopic perovskite solar cells, Surf. Interfaces 61 (2025) 106162. https://doi.org/10.1016/j.surfin.2025.106162.

[17] S. Bhandari, A. Roy, M.S. Ali, T.K. Mallick, S. Sundaram, Cotton soot derived carbon nanoparticles for NiO supported processing temperature tuned ambient perovskite solar cells, Sci. Rep. 11 (2021). https://doi.org/10.1038/s41598-021-02796-w.

[18] L. Zhou, Y. Zuo, T.K. Mallick, S. Sundaram, Enhanced Efficiency of Carbon-Based Mesoscopic Perovskite Solar Cells through a Tungsten Oxide Nanoparticle Additive in the Carbon Electrode, Sci. Rep. 9 (2019). https://doi.org/10.1038/s41598-019-45374-x.

[19] S. Bhandari, A. Roy, A. Ghosh, T.K. Mallick, S. Sundaram, Performance of WO_3-Incorporated Carbon Electrodes for Ambient Mesoscopic Perovskite Solar Cells, ACS Omega 5 (2020) 422–429. https://doi.org/10.1021/acsomega.9b02934.

[20] D. Wang, Q. Chen, H. Mo, D. Cheng, X. Liu, W. Liu, J. Jacobs, A.G. Thomas, Z. Liu, R.J. Curry, In situ laser generation of NiO nanoparticles embedded in graphene flakes for ambient-processed hole-transport-layer-free perovskite solar cells, Carbon 214 (2023) 118360. https://doi.org/10.1016/j.carbon.2023.118360.

[21] L. Ding, H. Tao, C. Zhang, J. Li, W. Zhang, J. Wang, J. Xue, P-type doping of rGO/NiO composite for carbon based perovskite solar cells, Mater. Sci. Semicond. Process. 107 (2020) 104798. https://doi.org/10.1016/j.mssp.2019.104798.

[22] L. Chu, W. Liu, Z. Qin, R. Zhang, R. Hu, J. Yang, J. Yang, X. Li, Boosting efficiency of hole conductor-free perovskite solar cells by incorporating p-type NiO nanoparticles into

carbon electrodes, Sol. Energy Mater. Sol. Cells 178 (2018) 164–169. https://doi.org/10.1016/j.solmat.2018.01.010.

[23] S. Bhandari, S. Valsalakumar, Y. Chanchangi, P. Selvaraj, T.K. Mallick, Effect of novel graphitic carbon/NiO hole transporting electrode on the photovoltaic and optical performance of semi-transparent perovskite solar cells, RSC Adv. 13 (2023) 7380–7384. https://doi.org/10.1039/d2ra08198a.

[24] Y. Gou, J. Zhang, B. Jin, W. Dai, W. Zhang, C. Chen, L. Lin, X. Wang, Q. Tai, J. Li, Work Function Tuning of Carbon Electrode to Boost the Charge Extraction in Hole Transport Layer-Free Perovskite Solar Cells, Small (2024). https://doi.org/10.1002/smll.202403342.

[25] Z. Golshani, F. Arjmand, S. Maghsoudi, S.M.A. Hosseini, Fe2O3–NiO doped carbon counter electrode for high-performance and long-term stable photovoltaic perovskite solar cells, J. Mater. Res. Technol. 23 (2023) 2612–2625. https://doi.org/10.1016/j.jmrt.2023.01.178.

[26] F.-W. Liu, G. Biesold, M. Zhang, R. Lawless, J.-P. Correa-Baena, Y.-L. Chueh, Z. Lin, Recycling and recovery of perovskite solar cells, Mater. Today 43 (2021) 185–197. https://doi.org/10.1016/j.mattod.2020.11.024.

[27] K. Valadez-Villalobos, C. Worsley, R. Garcia-Rodriguez, T. Watson, M. Davies, Sustainable remanufacturing of mesoscopic carbon perovskite solar cells using green solvents, RSC Sustain. 4 (2026) 754–759. https://doi.org/10.1039/d5su00707k.

[28] E.S. Akulenko, M. Hadadian, M. Esmaeilzadeh, R. Nizamov, K. Miettunen, BOTTLENECKS IN PEROVSKITE SOLAR CELL RECYCLING, (2023) 020106-001-020106–004. https://doi.org/10.4229/EUPVSEC2023/2BV.2.13.

[29] N.-G. Park, Perovskite solar cells: an emerging photovoltaic technology, Mater. Today 18 (2015) 65–72. https://doi.org/10.1016/j.mattod.2014.07.007.

[30] A. Kojima, K. Teshima, Y. Shirai, T. Miyasaka, Organometal Halide Perovskites as Visible-Light Sensitizers for Photovoltaic Cells, J. Am. Chem. Soc. 131 (2009) 6050–6051. https://doi.org/10.1021/ja809598r.

[31] H.-S. Kim, C.-R. Lee, J.-H. Im, K.-B. Lee, T. Moehl, A. Marchioro, S.-J. Moon, R. Humphry-Baker, J.-H. Yum, J.E. Moser, M. Grätzel, N.-G. Park, Lead Iodide Perovskite Sensitized All-Solid-State Submicron Thin Film Mesoscopic Solar Cell with Efficiency Exceeding 9%, Sci. Rep. 2 (2012) 591. https://doi.org/10.1038/srep00591.

[32] J. Burschka, N. Pellet, S.-J. Moon, R. Humphry-Baker, P. Gao, M.K. Nazeeruddin, M. Grätzel, Sequential deposition as a route to high-performance perovskite-sensitized solar cells, Nature 499 (2013) 316–319. https://doi.org/10.1038/nature12340.

[33] H. Zhou, Q. Chen, G. Li, S. Luo, T. Song, H.-S. Duan, Z. Hong, J. You, Y. Liu, Y. Yang, Interface engineering of highly efficient perovskite solar cells, Science 345 (2014) 542–546. https://doi.org/10.1126/science.1254050.

[34] B. Kang, F. Yan, Emerging strategies for the large-scale fabrication of perovskite solar modules: from design to process, Energy Environ. Sci. 18 (2025) 3917–3954. https://doi.org/10.1039/D4EE05613B.

[35] D. Zhang, D. Li, Y. Hu, A. Mei, H. Han, Degradation pathways in perovskite solar cells and how to meet international standards, Commun. Mater. 3 (2022) 58. https://doi.org/10.1038/s43246-022-00281-z.

[36] Microquanta Semiconductor, (n.d.). https://www.microquanta.com/#/v2/home/pc (accessed March 16, 2026).

[37] Vincent Shaw, Chinese developer switches on world's largest perovskite-based PV plant, (2024). https://www.pv-magazine.com/2024/12/09/chinese-developer-switches-on-worlds-largest-perovskite-based-pv-plant/ (accessed March 16, 2026).

[38] Vincent Shaw, Chinese PV Industry Brief: UtmoLight starts perosvkite module production, (2025). https://www.pv-magazine.com/2025/02/07/chinese-pv-industry-brief-utmolight-begins-perosvkite-solar-module-production-at-gw-scale-facility/ (accessed March 16, 2026).

[39] Vincent Shaw, UtmoLight unveils 450 W perovskite solar module with 16.1% efficiency, (2024). https://www.pv-magazine.com/2024/11/13/utmolight-unveils-450-w-perovskite-solar-module-with-16-1-efficiency/ (accessed March 16, 2026).

[40] Oxford PV, (n.d.). https://www.oxfordpv.com/ (accessed April 22, 2026).

[41] Emiliano Bellini, Eckhart Gouras, Oxford PV targets 20-year lifetime for perovskite-silicon tandem modules by 2028, PV Mag. (2026). https://www.pv-magazine.com/2026/01/16/oxford-pv-targets-20-year-lifetime-for-perovskite-silicon-tandem-modules-by-2028/ (accessed April 22, 2026).

[42] D. Walter, J. Peng, K. Weber, K.R. Catchpole, T.P. White, Performance limitations imposed by the TCO heterojunction in high efficiency perovskite solar cells, Energy Environ. Sci. 15 (2022) 5202–5216. https://doi.org/10.1039/D2EE01742C.

[43] Y. Xu, Z. Lin, W. Wei, Y. Hao, S. Liu, J. Ouyang, J. Chang, Recent Progress of Electrode Materials for Flexible Perovskite Solar Cells, Nano-Micro Lett. 14 (2022) 117. https://doi.org/10.1007/s40820-022-00859-9.

[44] G. Yang, H. Tao, P. Qin, W. Ke, G. Fang, Recent progress in electron transport layers for efficient perovskite solar cells, J. Mater. Chem. A 4 (2016) 3970–3990. https://doi.org/10.1039/C5TA09011C.

[45] D.P. McMeekin, G. Sadoughi, W. Rehman, G.E. Eperon, M. Saliba, M.T. Hörantner, A. Haghighirad, N. Sakai, L. Korte, B. Rech, M.B. Johnston, L.M. Herz, H.J. Snaith, A mixed-cation lead mixed-halide perovskite absorber for tandem solar cells, Science 351 (2016) 151–155. https://doi.org/10.1126/science.aad5845.

[46] S. Tao, I. Schmidt, G. Brocks, J. Jiang, I. Tranca, K. Meerholz, S. Olthof, Absolute energy level positions in tin- and lead-based halide perovskites, Nat. Commun. 10 (2019) 2560. https://doi.org/10.1038/s41467-019-10468-7.

[47] A. Walsh, Principles of Chemical Bonding and Band Gap Engineering in Hybrid Organic–Inorganic Halide Perovskites, J. Phys. Chem. C 119 (2015) 5755–5760. https://doi.org/10.1021/jp512420b.

[48] D. Bryant, N. Aristidou, S. Pont, I. Sanchez-Molina, T. Chotchunangatchaval, S. Wheeler, J.R. Durrant, S.A. Haque, Light and oxygen induced degradation limits the operational stability of methylammonium lead triiodide perovskite solar cells, Energy Environ. Sci. 9 (2016) 1655–1660. https://doi.org/10.1039/C6EE00409A.

[49] E. Smecca, Y. Numata, I. Deretzis, G. Pellegrino, S. Boninelli, T. Miyasaka, A. La Magna, A. Alberti, Stability of solution-processed $MAPbI_3$ and $FAPbI_3$ layers, Phys. Chem. Chem. Phys. 18 (2016) 13413–13422. https://doi.org/10.1039/C6CP00721J.

[50] K. Sakhatskyi, R.A. John, A. Guerrero, S. Tsarev, S. Sabisch, T. Das, G.J. Matt, S. Yakunin, I. Cherniukh, M. Kotyrba, Y. Berezovska, M.I. Bodnarchuk, S. Chakraborty, J. Bisquert, M.V. Kovalenko, Assessing the Drawbacks and Benefits of Ion Migration in Lead Halide Perovskites, ACS Energy Lett. 7 (2022) 3401–3414. https://doi.org/10.1021/acsenergylett.2c01663.

[51] ECHA, European Chemicals Agency, Lead, (n.d.). https://echa.europa.eu/hot-topics/lead (accessed April 5, 2026).

[52] W. Ke, M.G. Kanatzidis, Prospects for low-toxicity lead-free perovskite solar cells, Nat. Commun. 10 (2019) 965. https://doi.org/10.1038/s41467-019-08918-3.

[53] I. Ahmed, K. Prakash, S.M. Mobin, Lead-free perovskites for solar cell applications: recent progress, ongoing challenges, and strategic approaches, Chem. Commun. 61 (2025) 6691–6721. https://doi.org/10.1039/D4CC06835A.

[54] A. Krishna, A.C. Grimsdale, Hole transporting materials for mesoscopic perovskite solar cells – towards a rational design?, J. Mater. Chem. A 5 (2017) 16446–16466. https://doi.org/10.1039/C7TA01258F.

[55] Z. Li, C. Xiao, Y. Yang, S.P. Harvey, D.H. Kim, J.A. Christians, M. Yang, P. Schulz, S.U. Nanayakkara, C.-S. Jiang, J.M. Luther, J.J. Berry, M.C. Beard, M.M. Al-Jassim, K. Zhu, Extrinsic ion migration in perovskite solar cells, Energy Environ. Sci. 10 (2017) 1234–1242. https://doi.org/10.1039/C7EE00358G.

[56] J. Seo, S. Akin, M. Zalibera, M.A.R. Preciado, H. Kim, S.M. Zakeeruddin, J.V. Milić, M. Grätzel, Dopant Engineering for Spiro-OMeTAD Hole-Transporting Materials towards Efficient Perovskite Solar Cells, Adv. Funct. Mater. 31 (2021) 2102124. https://doi.org/10.1002/adfm.202102124.

[57] X. Chen, F. Zheng, Y. Hou, B. Yang, R. Zhao, G. Ma, J. Wu, S. Shafique, K.P. Ghiggino, Z. Hu, Guanidinium Iodide-Modified PEDOT:PSS Hole Transport Layer for Improving the Performance of 2D Perovskite Solar Cells, Langmuir 41 (2025) 10715–10725. https://doi.org/10.1021/acs.langmuir.5c01113.

[58] X. Fan, N.E. Stott, J. Zeng, Y. Li, J. Ouyang, L. Chu, W. Song, PEDOT:PSS materials for optoelectronics, thermoelectrics, and flexible and stretchable electronics, J. Mater. Chem. A 11 (2023) 18561–18591. https://doi.org/10.1039/D3TA03213B.

[59] Y. Wang, Y. Xu, J. Yun, Q. Cai, L. Zhai, D. Zhuang, G. Yang, H. Huang, M. Li, Y. Yang, L. Zhang, C. Zou, Suppressing interfacial nonradiative recombination by alkali hydroxides for efficient blue perovskite light-emitting diodes, Chem. Eng. J. 486 (2024) 149964. https://doi.org/10.1016/j.cej.2024.149964.

[60] Y.-C. Chin, M. Daboczi, C. Henderson, J. Luke, J.-S. Kim, Suppressing PEDOT:PSS Doping-Induced Interfacial Recombination Loss in Perovskite Solar Cells, ACS Energy Lett. 7 (2022) 560–568. https://doi.org/10.1021/acsenergylett.1c02577.

[61] V.D. Patel, D. Gupta, Solution-processed metal-oxide based hole transport layers for organic and perovskite solar cell: A review, Mater. Today Commun. 31 (2022) 103664. https://doi.org/10.1016/j.mtcomm.2022.103664.

[62] K.M. Anoop, T.N. Ahipa, Recent advancements in the hole transporting layers of perovskite solar cells, Sol. Energy 263 (2023) 111937. https://doi.org/10.1016/j.solener.2023.111937.

[63] R. Chen, W. Zhang, X. Guan, H. Raza, S. Zhang, Y. Zhang, P.A. Troshin, S.A. Kuklin, Z. Liu, W. Chen, Rear Electrode Materials for Perovskite Solar Cells, Adv. Funct. Mater. 32 (2022) 2200651. https://doi.org/10.1002/adfm.202200651.

[64] Y. Kato, L.K. Ono, M.V. Lee, S. Wang, S.R. Raga, Y. Qi, Silver Iodide Formation in Methyl Ammonium Lead Iodide Perovskite Solar Cells with Silver Top Electrodes, Adv. Mater. Interfaces 2 (2015) 1500195. https://doi.org/10.1002/admi.201500195.

[65] K. Domanski, J.-P. Correa-Baena, N. Mine, M.K. Nazeeruddin, A. Abate, M. Saliba, W. Tress, A. Hagfeldt, M. Grätzel, Not All That Glitters Is Gold: Metal-Migration-Induced Degradation in Perovskite Solar Cells, ACS Nano 10 (2016) 6306–6314. https://doi.org/10.1021/acsnano.6b02613.

[66] L. Zhao, R.A. Kerner, Z. Xiao, Y.L. Lin, K.M. Lee, J. Schwartz, B.P. Rand, Redox Chemistry Dominates the Degradation and Decomposition of Metal Halide Perovskite Optoelectronic Devices, ACS Energy Lett. 1 (2016) 595–602. https://doi.org/10.1021/acsenergylett.6b00320.

[67] J. He, Y. Bai, Z. Luo, R. Ran, W. Zhou, W. Wang, Z. Shao, Advanced carbon-based rear electrodes for low-cost and efficient perovskite solar cells, Energy Environ. Sci. 18 (2025) 2136–2164. https://doi.org/10.1039/d4ee05462h.

[68] X. Huang, B. Wu, N. Zheng, Optimizing Solvent Chemistry for High-Quality Halide Perovskite Films, Acc. Mater. Res. 6 (2025) 40–51. https://doi.org/10.1021/accountsmr.4c00148.

[69] L. Wagner, C. Qiu, M. Unmüssig, D. Bogachuk, S. Mastroianni, U. Würfel, Y. Hu, H. Han, A. Hinsch, A 2D Model for Interfacial Recombination in Mesoscopic Perovskite Solar Cells with Printed Back Contact, Sol. RRL 5 (2021) 2000595. https://doi.org/10.1002/solr.202000595.

[70] H. Chen, S. Yang, Carbon-Based Perovskite Solar Cells without Hole Transport Materials: The Front Runner to the Market?, Adv. Mater. 29 (2017) 1603994. https://doi.org/10.1002/adma.201603994.

[71] R. Smith, Directive 2010/41/EU of the European Parliament and of the Council of 7 July 2010, in: Core EU Legis., Macmillan Education UK, London, 2015: pp. 352–355. https://doi.org/10.1007/978-1-137-54482-7_33.

[72] F. Kerkel, M. Markiewicz, S. Stolte, E. Müller, W. Kunz, The green platform molecule gamma-valerolactone – ecotoxicity, biodegradability, solvent properties, and potential applications, Green Chem. 23 (2021) 2962–2976. https://doi.org/10.1039/D0GC04353B.

[73] C. Worsley, D. Raptis, S. Meroni, A. Doolin, R. Garcia-Rodriguez, M. Davies, T. Watson, γ-Valerolactone: A Nontoxic Green Solvent for Highly Stable Printed Mesoporous Perovskite Solar Cells, Energy Technol. 9 (2021) 2100312. https://doi.org/10.1002/ente.202100312.

[74] P. Kajal, J.H. Lew, A. Kanwat, P.J.S. Rana, G.V. Nutan, T.M. Koh, S.G. Mhaisalkar, S. Powar, N. Mathews, Unveiling the role of carbon black in printable mesoscopic perovskite solar cells, J. Power Sources 501 (2021) 230019. https://doi.org/10.1016/j.jpowsour.2021.230019.

[75] L. Zhang, T. Liu, L. Liu, M. Hu, Y. Yang, A. Mei, H. Han, The effect of carbon counter electrodes on fully printable mesoscopic perovskite solar cells, J. Mater. Chem. A 3 (2015) 9165–9170. https://doi.org/10.1039/C4TA04647A.

[76] R. Tsuji, K. Tanaka, K. Oishi, T. Shioki, H. Satone, S. Ito, Role and Function of Polymer Binder Thickeners in Carbon Pastes for Multiporous-Layered-Electrode Perovskite Solar Cells, Chem. Mater. 35 (2023) 8574–8589. https://doi.org/10.1021/acs.chemmater.3c01483.

[77] M. Forouzandeh, M. Heidariramsheh, H.R. Heydarnezhad, H. Nikbakht, M. Stefanelli, L. Vesce, N. Taghavinia, Enhanced carbon-based back contact electrodes for perovskite solar cells: Effect of carbon paste composition on performance and stability, Carbon 229 (2024) 119450. https://doi.org/10.1016/j.carbon.2024.119450.

[78] B. Xu, D. Liu, C. Dong, M. Awais, W. Wang, Y. Song, Y. Deng, M. Yao, J. Tong, G. Yue, W. Zhang, F. Tan, M.I. Saidaminov, NiOx for interface and work function engineering in carbon-based all-inorganic perovskite solar cells, J. Colloid Interface Sci. 641 (2023) 105–112. https://doi.org/10.1016/j.jcis.2023.03.049.

[79] D. Bogachuk, P. Van Der Windt, L. Wagner, D. Martineau, S. Narbey, A. Verma, J. Lim, S. Zouhair, M. Kohlstädt, A. Hinsch, S.D. Stranks, U. Würfel, S.W. Glunz,

Remanufacturing Perovskite Solar Cells and Modules–A Holistic Case Study, ACS Sustain. Resour. Manag. 1 (2024) 417–426. https://doi.org/10.1021/acssusresmgt.3c00042.

[80] D. Bogachuk, S. Zouhair, K. Wojciechowski, B. Yang, V. Babu, L. Wagner, B. Xu, J. Lim, S. Mastroianni, H. Pettersson, A. Hagfeldt, A. Hinsch, Low-temperature carbon-based electrodes in perovskite solar cells, Energy Environ. Sci. 13 (2020) 3880–3916. https://doi.org/10.1039/D0EE02175J.

[81] Q. Gao, X. Li, J. Liu, K. Chen, X. Xiao, X. Wang, J. Xiang, A. Mei, H. Han, Defect-Rich Boron-Doped Graphite for High-Performance Hole-Conductor-Free Mesoscopic Perovskite Solar Cells with Enhanced Back Interface Contact, ACS Mater. Lett. 6 (2024) 3025–3033. https://doi.org/10.1021/acsmaterialslett.4c00799.

[82] M. Chen, R.-H. Zha, Z.-Y. Yuan, Q.-S. Jing, Z.-Y. Huang, X.-K. Yang, S.-M. Yang, X.-H. Zhao, D.-L. Xu, G.-D. Zou, Boron and phosphorus co-doped carbon counter electrode for efficient hole-conductor-free perovskite solar cell, Chem. Eng. J. 313 (2017) 791–800. https://doi.org/10.1016/j.cej.2016.12.050.

[83] C. Tian, A. Mei, S. Zhang, H. Tian, S. Liu, F. Qin, Y. Xiong, Y. Rong, Y. Hu, Y. Zhou, S. Xie, H. Han, Oxygen management in carbon electrode for high-performance printable perovskite solar cells, Nano Energy 53 (2018) 160–167. https://doi.org/10.1016/j.nanoen.2018.08.050.

[84] M. Duan, C. Tian, Y. Hu, A. Mei, Y. Rong, Y. Xiong, M. Xu, Y. Sheng, P. Jiang, X. Hou, X. Zhu, F. Qin, H. Han, Boron-Doped Graphite for High Work Function Carbon Electrode in Printable Hole-Conductor-Free Mesoscopic Perovskite Solar Cells, ACS Appl. Mater. Interfaces 9 (2017) 31721–31727. https://doi.org/10.1021/acsami.7b05689.

[85] Y. Shi, X. Cheng, Y. Wang, W. Li, W. Shang, W. Liu, W. Lu, J. Cheng, L. Liu, Y. Shi, Atomically Dispersed Metal Atoms: Minimizing Interfacial Charge Transport Barrier for Efficient Carbon-Based Perovskite Solar Cells, Nano-Micro Lett. 17 (2025) 125. https://doi.org/10.1007/s40820-024-01639-3.

[86] R. Hu, R. Zhang, Y. Ma, W. Liu, L. Chu, W. Mao, J. Zhang, J. Yang, Y. Pu, X. Li, Enhanced hole transfer in hole-conductor-free perovskite solar cells via incorporating CuS into carbon electrodes, Appl. Surf. Sci. 462 (2018) 840–846. https://doi.org/10.1016/j.apsusc.2018.08.078.

[87] E. Barruna, A. Saniah, S.F. Rahman, N.R. Poespawati, Material Characteristics and Electrical Performance of Perovskite Solar Cells with Different Carbon-Based Electrodes Mixed with CuSCN, J. Electr. Comput. Eng. 2023 (2023) 1–11. https://doi.org/10.1155/2023/8931693.

[88] J. Han, X. Yin, Y. Zhou, H. Nan, Y. Gu, M. Tai, J. Li, H. Lin, High Efficient Large-area Perovskite Solar Cells Based on Paintable Carbon Electrode with NiO Nanocrystal-carbon Intermediate Layer, Chem. Lett. 48 (2019) 734–737. https://doi.org/10.1246/cl.190210.

[89] Tulus, L.A. Muscarella, Y. Galagan, S.C. Boehme, E. Von Hauff, Trap passivation and suppressed electrochemical dynamics in perovskite solar cells with C60 interlayers, Electrochimica Acta 433 (2022) 141215. https://doi.org/10.1016/j.electacta.2022.141215.

[90] F. Ebadi, N. Taghavinia, R. Mohammadpour, A. Hagfeldt, W. Tress, Origin of apparent light-enhanced and negative capacitance in perovskite solar cells, Nat. Commun. 10 (2019) 1574. https://doi.org/10.1038/s41467-019-09079-z.

[91] W. Clarke, G. Richardson, P. Cameron, Understanding the Full Zoo of Perovskite Solar Cell Impedance Spectra with the Standard Drift-Diffusion Model, Adv. Energy Mater. 14 (2024) 2400955. https://doi.org/10.1002/aenm.202400955.

[92] E. Von Hauff, D. Klotz, Impedance spectroscopy for perovskite solar cells: characterisation, analysis, and diagnosis, J. Mater. Chem. C 10 (2022) 742–761. https://doi.org/10.1039/D1TC04727B.

[93] Solaronix, (n.d.). https://www.solaronix.com/ (accessed May 13, 2026).

[94] L. Wang, G.-H. Zhang, K.-C. Chou, Study on oxidation mechanism and kinetics of MoO2 to MoO3 in air atmosphere, Int. J. Refract. Met. Hard Mater. 57 (2016) 115–124. https://doi.org/10.1016/j.ijrmhm.2016.03.001.

[95] Kahruman, C., I. Yusufoglu, and E. Oktay., Kinetics of oxidation of MoO 2 to MoO 3 by oxygen at elevated temperatures, (1999).

[96] C. Qiu, J. Liu, S. Yang, D. Yan, L. Wagner, Y. Hu, Exploring the Impedance Spectroscopy in Hole-Conductor-Free Mesoscopic Perovskite Solar Cells, Prog. Photovolt. Res. Appl. (2025) pip.70047. https://doi.org/10.1002/pip.70047.

[97] D. Moia, I. Gelmetti, P. Calado, W. Fisher, M. Stringer, O. Game, Y. Hu, P. Docampo, D. Lidzey, E. Palomares, J. Nelson, P.R.F. Barnes, Ionic-to-electronic current amplification

in hybrid perovskite solar cells: ionically gated transistor-interface circuit model explains hysteresis and impedance of mixed conducting devices, Energy Environ. Sci. 12 (2019) 1296–1308. https://doi.org/10.1039/C8EE02362J.

[98] S. Zouhair, C. Clegg, I. Valitova, S. March, J.M. Jailani, V. Pecunia, Carbon Electrodes for Perovskite Photovoltaics: Interfacial Properties, Meta-analysis, and Prospects, Sol. RRL 8 (2024) 2300929. https://doi.org/10.1002/solr.202300929.

[99] J. Zhao, X. Zheng, Y. Deng, T. Li, Y. Shao, A. Gruverman, J. Shield, J. Huang, Is Cu a stable electrode material in hybrid perovskite solar cells for a 30-year lifetime?, Energy Environ. Sci. 9 (2016) 3650–3656. https://doi.org/10.1039/C6EE02980A.

[100] K.A. Khawaja, W. Xiang, J. Wall, X. Gu, L. Li, F. Yan, Hole transport layer selection for stable and efficient carbon electrode-based perovskite solar cells, RSC Adv. 15 (2025) 13681–13690. https://doi.org/10.1039/D5RA01694K.